Powder Technology 407 (2022) 117688

Contents lists available at ScienceDirect

Powder Technology

journal homepage: www.journals.elsevier.com/powder-technology

# Simulation and validation of the gas flow in close-coupled gas atomisation process: Influence of the inlet gas pressure and the throat width of the supersonic gas nozzle

Ernesto Urionabarrenetxea [a,b,*], José Manuel Martín [a,b], Alejo Avello [a,b], Alejandro Rivas [b]

[a] CEIT-Basque Research and Technology Alliance (BRTA), Manuel Lardizabal 15, 20018 Donostia/San Sebastián, Spain
[b] Universidad de Navarra, Tecnun, Manuel Lardizabal 13, 20018 Donostia/San Sebastián, Spain

## HIGHLIGHTS

- Simulated gas flow dynamics validated by Particle Image Velocimetry.
- Adjusting the pressure inlet, similar gas flows result with different gas atomisers.
- Longer supersonic plumes are obtained increasing the inlet atomising pressure.
- The gas consumption value combines the effect of the pressure and the gas atomiser.
- The numerical data explain the resulting particle size distributions of the powders.

## GRAPHICAL ABSTRACT

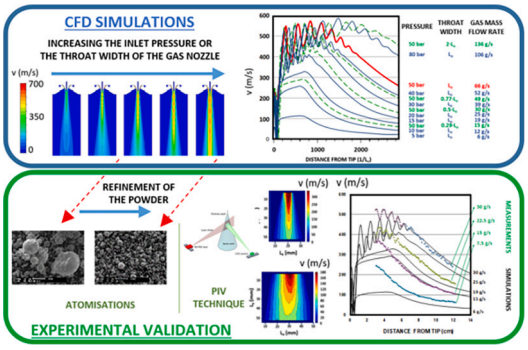


## ARTICLE INFO

*Keywords:*
Gas atomisation
Computational fluid dynamics
Close-coupled atomiser
Convergent-divergent gas nozzle
Metal powders
Particle image velocimetry

## ABSTRACT

The effectiveness of a close-coupled gas atomisation process largely depends on the operational and the geometric variables. In this study, Computational Fluid Dynamics (CFD) techniques are used to model and simulate the gas flow in the melt nozzle area for a convergent-divergent, close-coupled gas atomiser in the absence of the melt stream. Firstly, a reference case, in which the atomisation gas is nitrogen at 50 bar and a supersonic gas nozzle with a throat width of $L_0$ has been modelled, is presented. Then, the influence of both the inlet gas pressure and this design parameter are investigated, comparing the numerical results provided by simulations varying the inlet pressure from 5 to 80 bar and modelling different convergent-divergent gas nozzles with throat widths of $0.29 \bullet L_o$, $0.5 \bullet L_o$, $0.77 \bullet L_o$ and $2 \bullet L_o$ respectively. The simulation results show how similarly these two parameters modify gas mass flow rates, gas velocity fields, aspiration pressures in the melt delivery tube or the size of the recirculation zones below the melt nozzle. Therefore, it can be stated that this geometric variable of the gas nozzle may be as relevant as the inlet pressure in the atomisation process. The most important novelty of this study is related to experimental validation of the numerical results using the Particle Image Velocimetry (PIV) technique and through direct measurements of gas mass flow rates, with a clear correlation between simulated and measured data. Moreover, some results obtained with experimental atomisations using copper and nitrogen are also presented. The experimental results show that finer powders are produced by increasing the

* Corresponding author at: CEIT-Basque Research and Technology Alliance (BRTA), Manuel Lardizabal 15, 20018 Donostia/San Sebastián, Spain.
*E-mail addresses:* eugomez@ceit.es (E. Urionabarrenetxea), jmmartin@ceit.es (J.M. Martín), alavello@ceit.es (A. Avello), arivas@tecnun.es (A. Rivas).

https://doi.org/10.1016/j.powtec.2022.117688
Received 2 May 2022; Received in revised form 23 June 2022; Accepted 28 June 2022
Available online 3 July 2022

atomising pressure or the throat width of the supersonic gas nozzle, which can be directly related to the gas flow dynamics calculated numerically.

## 1. Introduction

Metal powders are the basis of the Powder Metallurgy industry, which comprises of many processes to produce components with characteristics tailored to a specific application, such as near-net-shape, controlled porosity, specific functionalities and properties (e.g. mechanical, thermal, electrical, magnetic, etc.), or low price. The powders produced by different manufacturing processes are pre-conditioned (e.g. by heat treating, sieving, mixing, milling, etc.), consolidated (e.g. by press and sintering, hot pressing, hot isostatic pressing, etc.) and subjected to subsequent finishing processes (e.g. heat treating, machining, coating, etc.) [1–3]. In recent decades, metal Additive Manufacturing (AM) has generated great interest because it allows geometrically complex objects to be obtained and enables rapid prototyping of parts. It is a technology that produces three-dimensional parts by repeated layer deposition, as opposed to traditional manufacturing methodologies, which are based on material subtraction [4]. Although some systems employ a solid wire feed, most commercial methods use metal powder, whose morphology serves as a key component in the final quality of the printed part [5,6]. The most predominant method for producing powder for metal AM is the gas atomisation process, given its suitable balance between production volume, morphology and particle size [7].

Gas atomisation is an effective and widely used process to produce fine spherical metal powders and it is attractive because of its easy application to several materials with good process control. In this process, a high-speed gas is used to break up a molten stream, thus transferring kinetic energy from the gas to the liquid metal stream, which then becomes unstable. Due to its lower cost, nitrogen is the preferred choice. When atomising materials reactive with nitrogen, argon is usually employed. The use of helium is expensive, but its high thermal conductivity enhances the cooling rate of the particles, helping to obtain amorphous structures [8]. The gas expanding around the molten stream causes a dramatic depressurization and the disintegration of the liquid. In the primary atomisation, the liquid column is broken into large droplets or ligaments by the expanding gas (Fig. 1). These large droplets disintegrate further during the secondary atomisation, forming smaller droplets that finally solidify in flight.

The most common gas atomiser designs are the close-coupled and free-fall types. The underlying difference between these two technologies is the location of the gas-melt interaction zone. The gas exit is next to the melt nozzle exit in close-coupled atomisation, while in free-fall atomisers, a distance between 10 cm and 30 cm is maintained between them. This distance allows the liquid metal to flow downward in quiescent atmosphere before the high velocity gas interacts with it. Despite the drawbacks of backflow and freeze-off that normally do not occur during free-fall atomisation, close-coupled atomisers are able to produce finer powders because the shorter distance favours the transfer of energy. Up until now, two different gas nozzles have been widely used for close-coupled atomisation, namely the annular-slit and the discrete-jet nozzle. The annular-slit nozzle is an annular slot surrounding the melt feeding tube, while the discrete-jet nozzle is made up of a number of discrete holes. The annular-slit nozzles are more widely used by industry due to their superior performance in comparison with the discrete-jet ones. The CEIT-BRTA research centre is equipped with a Phoenix Scientific Industries Ltd. small-scale research atomisation unit, model HERMIGA 75/3VI, whose atomiser is a close-coupled gas atomiser with an annular-slit nozzle as illustrated in Fig. 1.

The influence of the processing variables is best understood in terms of their capacity to affect the energy delivered to the melt. Any change from one atomisation to another has an impact on the resulting powders since their characteristics depend on several operational variables, geometrical parameters and physicochemical properties of the gas and the melt. In general, a higher gas-to-melt mass flow rates ratio (GMR) results in a finer powder. As atomisations can be performed with several gases at different inlet pressures or even with slightly different gas atomisers, gas velocity and gas mass flow rates can be changed. On the other hand, the melt mass flow rate can be adjusted through the melt stream diameter and by pressurizing the melting chamber. . Superheating the melt decreases its viscosity and prolongs the post-atomisation solidification time, helping to produce smaller spherical particles too.

Since the gas flow is the driving force in the breakup process, gaining insight into its dynamics is of paramount importance to understand the atomisation process. Computational Fluid Dynamics (CFD) is a brand

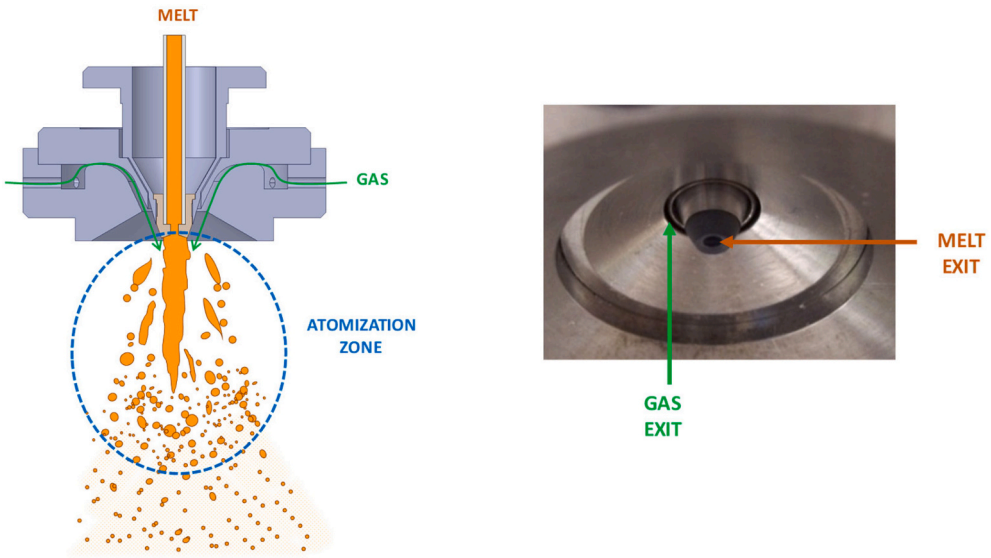


**Fig. 1.** Schematic diagram of the primary atomisation of a melt stream by the rapidly expanding gas (left) and photograph showing the proximity between the gas and the melt exits (right).

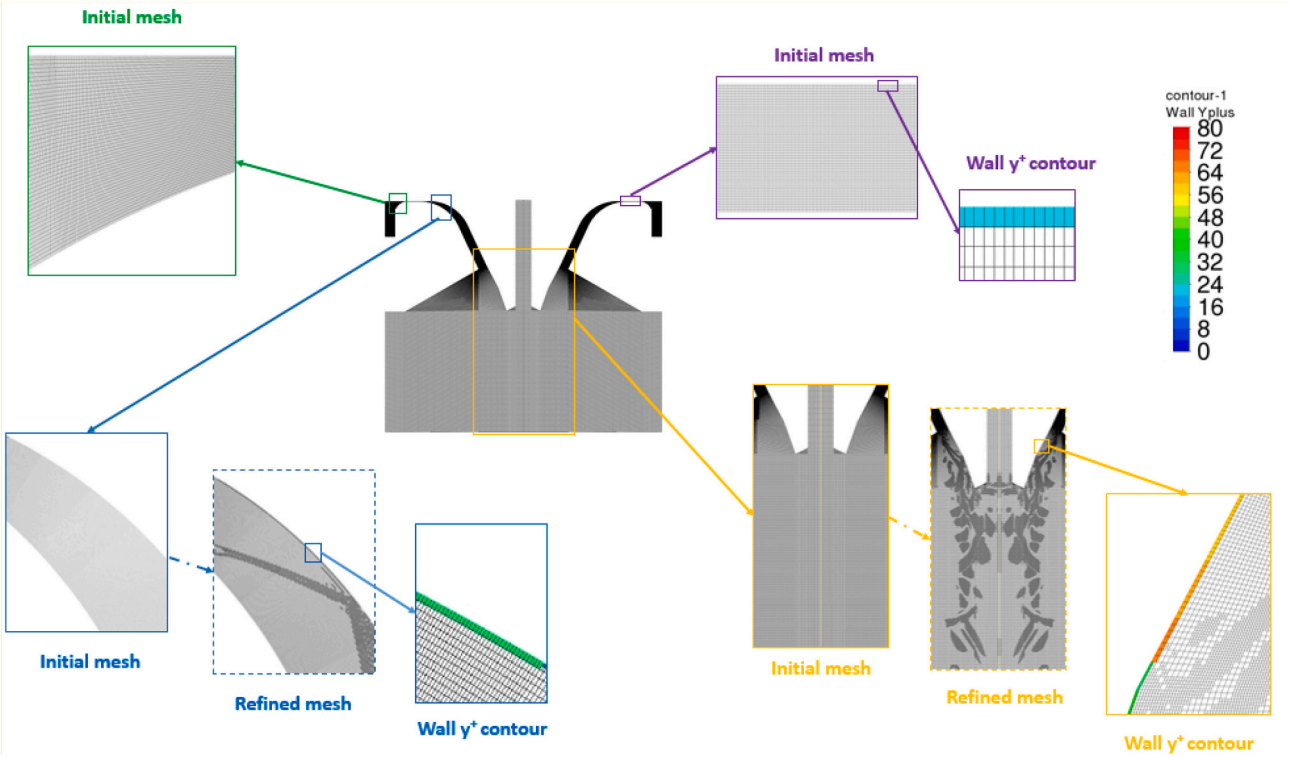


**Fig. 2.** Spatial discretization of the model and $y^+$ contours in some walls.

branch of fluid mechanics that uses numerical analysis and data structures to analyse and solve problems involving fluid flows as complex as the mixing efficiency in a micromixer module [9], the aerodynamic noise radiation from different rotor blade profiles [10] or the influence of the dry ice blasting nozzle geometry [11–14]. Various highly complex phenomena occurring during the gas atomisation process can also be modelled and simulated using CFD techniques. Simulations reveal details of the flow that are not experimentally accessible, but that have an impact on the powder properties. The majority of the previous studies simulate the gas flow dynamics in the absence of the liquid metal in order to understand the influence of certain operational and design variables on the atomisation process [15–22]. For example, Mi et al. [15] found that higher inlet pressures produce longer supersonic gas plumes, whereas Mates et al. [17] compared numerically the efficiency of different gas nozzle geometries. Ting and Anderson [18] conducted an investigation on the gas dynamics of the open-wake and closed-wake conditions to validate the predictions of a pulsatile atomisation model earlier proposed by Ting [23]. Zeoli et al. [19] proposed the concept of isentropic plug nozzles to reduce the shocks and maximize the kinetic energy transferred from the gas to destabilize the melt stream,showing also that preheating the atomising gas considerably reduces its consumption and produces greater velocities . Li et al. [20] revealed that the convergent-divergent nozzle expands the gas to a pressure very similar to the ambient pressure, so supersonic velocities are reached at the exit. In contrast, the convergent nozzle provides a highly sub-expanded and sonic flow, as well as a strong overpressure around the melt tip. Aydin and Ünal [22] proved that CFD simulations provide an accurate estimation of the actual aspiration pressure and that further increases of the gas pressure produce higher gas flow rates but not a significant increase in velocity magnitudes in the supersonic regime.

More complex studies are based on simulating only the secondary atomisation stage, as well as the solidification and cooling of liquid droplets during their flight time in the atomisation chamber, by means of Lagrangian Particle Tracking (LPT) [24–26]. In these studies, the injection points and initial diameters of the droplets are not derived from simulations of the primary atomisation so they are often chosen arbitrarily. However, a later study has demonstrated that the characteristics of the particle injection significantly affects the resulting particle size distributions [27]. Due to the inherently complex interaction between two fluids with extreme differences in terms of physical properties and time and length scales, there are only few studies modelling the primary atomisation stage of this metal production process [28–30]. Thus, accurate modelling of the transition from primary to secondary atomisation remains a challenge. In recent years, several multiphase models have been developed to simulate the disintegration of other liquids such as water and fuels, where Eulerian–Lagrangian (EL) approaches have taken on a leading role. They are mostly based on Interface Capturing Methods (ICM) in Eulerian models for the dense part of the spray, and then switching to LPT in the dilute region (ICM + LPT). A substantial amount of literature is available on this topic, proposing models that differ from the Eulerian model and transition criteria [31–34]. Although considerable advances have been made, EL transition models demand excessive computing power for current average computers. In the particular case of close-coupled gas atomisation, the calculation time required for reaching a statistically steady state is long. Furthermore, the presence of shock waves and the thermal nonequilibrium between phases lead to a highly unsteady process, giving rise to additional numerical constraints. These limitations encourage simplified multiphase models such as the Eulerian Spray Atomisation (ESA) or the Eulerian–Lagrangian Spray Atomisation (ELSA) models to be considered [4,35,36].

Although recent studies focus primarily on developing new multiphase models to study the interaction between the atomising gas and the melt liquid, the authors of this study ensure that highly valuable information can be extracted from single-phase simulations. Nowadays, the main challenges faced by the gas atomisation process is finding the optimum combination of operational and geometrical parameters that maximizes yield, while overcoming the natural tendency to produce wide particle size distributions and avoiding the satellite formation and particle aggregation [37–41]. Since the main cause of the latter is the

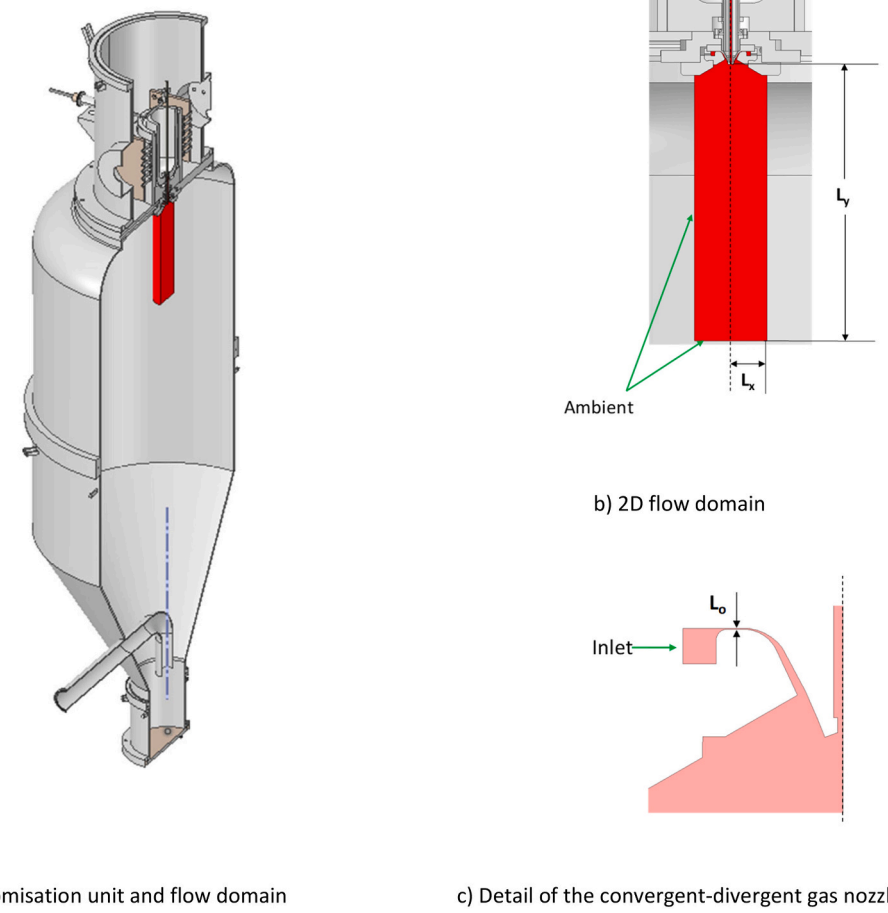


**Fig. 3.** Flow domain and boundary conditions imposed on the model.

recirculation of solidified fine particles in the atomisation chamber and these surface defects reduce the flowability of the atomised powders [42,43] the use of anti-satellite systems is recommended [44,45]. However, the reason for the former is still not fully understood. Thus, the gas atomiser design optimisation is a really interesting topic at present, which can be approached, in a faster way, simulating only the atomising gas flow dynamics instead of performing more complex multiphase simulations. The simulations in this work model the gas flow in the absence of the metal stream using axisymmetric two-dimensional models Unlike other studies, which use simplified geometries, an accurate geometric model of the gas nozzle is used here, ensuring that no simplifications in those aspects that could affect the gas dynamics. Several simulations were specifically designed to understand the influence of the inlet gas pressure and the throat width of the supersonic gas nozzle. The numerical results have shown that any small variation in its length produce important effects on the resulting gas flow characteristics due to the reduced size of this geometric variable. It is demonstrated that its influence may be assimilated to that of the inlet gas pressure, which has always been considered predominant in the gas atomisation process. However, it can be stated that the most important novelty of this study is related to the validation process followed after performing the CFD simulations since there is a clear lack of experimental validation of them. The numerical results have been experimentally validated by Particle Image Velocimetry (PIV), which is a very unusual technique in the context of the gas atomisation process, and gas mass flow measurements. Although PIV technique has been used in other cases related to AM technologies [46,47], to the best of the authors' knowledge, there is only one article in literature where this complex technique was used in connection with the gas atomisation process [16]. It was employed to measure the size and the velocity of copper droplets during the atomisation itself, while this equipment has been selected to measure the velocity of the atomising gas in order to validate the results provided by the CFD simulations. Due to the clear correlation between the numerical results and the experimental measurements in both axial and radial directions, it is confirmed that the simulations are capable of correctly predicting the atomising gas flow inside the atomisation chamber. Consequently, CFD techniques are a very suitable tool to advance in the design of more efficient gas atomisers [48]. Finally, the relevant powder properties of copper powders atomised experimentally are explained by means of the simulation results.

## 2. Modelling and simulation procedure

The gas flow inside the atomisation chamber in the absence of the melt stream has been modelled and simulated through the commercial code Ansys Fluent 2021 R1. The ideal flow domain would be one that would permit a detailed study of the atomising gas flow from the gas supply to the exterior. Fig. 2.a displays the complete geometry of the atomisation unit. However, this option is not feasible due to the excessive size of the domain, the associated computational cost and the difficulty in performing a fine enough spatial discretization to capture all the gas dynamics. In addition, this flow domain would have to be considered as three-dimensional and tridirectional, so that no component in the velocity field or any spatial coordinate could be obviated. Consequently, a series of decisions have been made to limit the flow domain in the mathematical model. Due to the rotational symmetry of

both the atomisation unit and the boundary conditions, an axisymmetric model of one half of a meridional section is considered, which comprises of a section before the gas nozzle, the supersonic gas nozzle itself and a portion of the atomisation chamber (see Fig. 2.b). The width of the supersonic gas nozzle $L_o$, shown in Fig. 2.c, is considered to be the characteristic length of the model. Different domains varying the dimensions $L_x$ and $L_y$, marked in Fig. 2.b, were analysed in order to decide which size was the most suitable for performing the simulations. Finally, it was decided that a computational domain encompassing the gas flow field of $4285 \bullet L_o$ x $571 \bullet L_o$ would be used. Smaller domains ($1428 \bullet L_o$ x $286 \bullet L_o$, $2857 \bullet L_o$ x $286 \bullet L_o$ and $2857 \bullet L_o$ x $571 \bullet L_o$) gave convergence problems, while larger domains ($4285 \bullet L_o$ x $1142 \bullet L_o$ and $5714 \bullet L_o$ x $857 \bullet L_o$) delivered practically identical results to the $4285 \bullet L_o$ x $571 \bullet L_o$ domain. Due to the lower computational cost associated, these dimensions were taken as reference in all simulations.

The remarkable dimensional differences between the distinct zones are clearly observable in Fig. 2. While the part of the domain corresponding to the atomisation chamber has a total size of $4285 \bullet L_o$ x $571 \bullet L_o$, the dimensions of the convergent-divergent nozzle through which the atomising gas is expanded, hence increasing its kinetic energy, are much smaller (in the range of $\sim 180 \bullet L_o$ x $18 \bullet L_o$, with a minimum thickness at the throat of $L_o$). These dimensional differences have conditioned the spatial discretization of the model because the mesh should be fine enough across the large gradients and adjacent to geometrical changes to make sure that it is able to capture the high-velocity gas dynamics. It is essential to maintain an optimum mesh quality for consistency and stability of the solution [11–14].Since the structured quadrilateral mesh can provide better results at higher-order schemes and still retains better numerical stability and accuracy than the unstructured triangular mesh, it was necessary to partition the domain in order to create such a grid practically throughout the entire domain. Initially, the flow domain was divided into approximately 2.4 million. However, further local refinements in regions with high pressure and velocity gradients increased the final mesh to approximately 3 million cells in order to obtain a better resolution and achieve a good convergence cells (see Fig. 2). It was assumed that the discretization error was small when no variation in the results was detected after subsequent mesh refinements.

In the performed simulations, the flow is considered in steady state conditions. The atomising gas is nitrogen, which is treated as an ideal gas. Since the flow is in turbulent regimen, the Favre Averaged Navier Stokes (FANS) equations are solved using the turbulent viscosity approach for the closure of the flow and energy equations (see Appendix B). The turbulent viscosity is calculated through the Realizable $k - \epsilon$ model, and the employed treatment of the turbulence near the walls is a combination of a two-layer model with enhanced wall functions. The restriction that the near-wall mesh must be sufficiently fine to correctly assess the turbulence near the walls would have imposed too large a computational requirement. In order to have a near-wall formulation that possess the accuracy of the standard two-layer approach for fine meshes and that, at the same time, will not significantly reduce accuracy for coarse meshes, ANSYS Fluent provides the Enhanced Wall Treatment approach. It is a near-wall modeling method that highly decreases the error incurred for intermediate meshes, in which the first near-wall node is placed neither in the fully turbulent region (where the wall functions are suitable) nor in the direct vicinity of the wall (typically with the first near-wall node placed at $y^+ \sim 1$). The $y^+$ values are important inside the supersonic gas nozzle and other phenomena such as shock waves and flow detachments also occur there, which made it necessary a refinement of the initial mesh. As shown in Fig. 2, the mesh does not satisfy the $y^+ < 1$ criteria so the boundary layer flow cannot be resolved directly without wall functions [10,14]. Consequently, the Enhanced wall Treatment has been employed in this study.

The boundary conditions, which are indicated in Fig. 3.b and 3.c, consist of an inlet, ambient, a symmetry axis and adiabatic walls. The axis boundary condition is indispensable in the two-dimensional axisymmetric models. At the inlet, the values of both the total pressure and gas temperature must be entered, which are known thanks to the pressure regulator gauge and the temperature measurements taken with a thermocouple. In addition, a turbulent intensity of 1% and a turbulent viscosity ratio of 5 are set to characterize the incoming gas turbulence. The atmospheric pressure value is fixed at the pressure outlet boundary condition, as it is assumed that the atomising gas must be fully expanded at such distances . As the gas is also entering the computational domain through a large part of this boundary due to the gas entrainment caused by the main inlet jet, it is also necessary to specify here the entrainment conditions. In this study, a backflow turbulent intensity of 1% and a backflow turbulent viscosity ratio of 5 are used. The rest of lines, not indicated in Fig. 3, which delimit the contour of the domain correspond to physical walls. The non-slip condition is imposed on these walls and they are also considered to be adiabatic.

The discrete mathematical model of the flow is obtained using the Finite Volume Method and second order schemes are used to discretize the source, convective and diffuse terms in the mass, momentum, and energy equations. The mass flow rates on the faces of the cells are obtained using a momentum interpolation. The pressure is considered unknown in the mathematical model (Pressure-based) and the density is obtained as a function of pressure and temperature using the state-

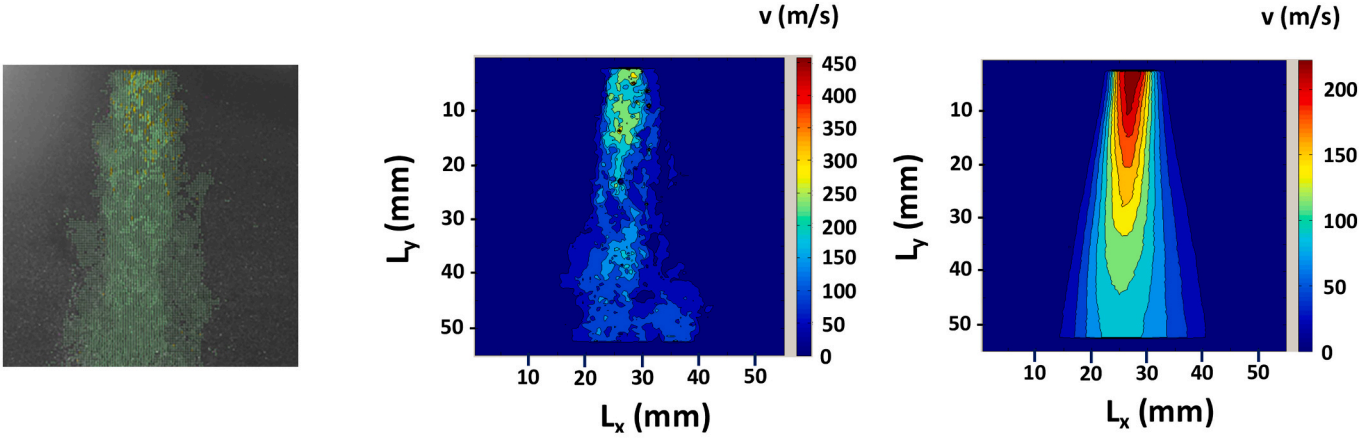


**Fig. 4.** Different fields obtained with the PIV technique.

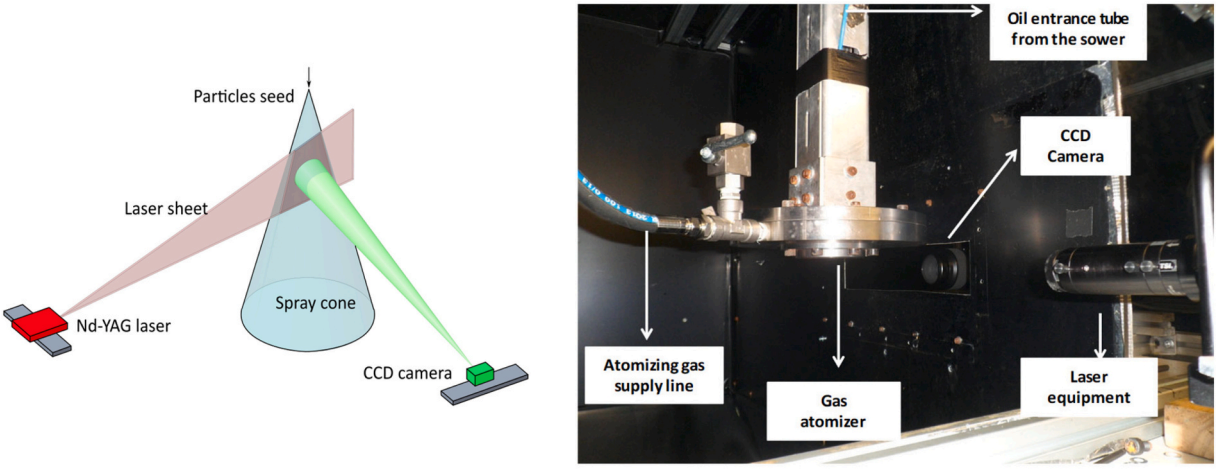


a) Scheme of the PIV measurement setup b) Photograph of the interior of the test bench

**Fig. 5.** PIV experimental measurements setup.

equation. The discrete mathematical model is solved in a segregate and iterative way using the SIMPLE algorithm, to couple the pressure and the velocity calculation, and the Gauss-Seidel method, which was accelerated with a multigrid scheme and Full Multi Grid initialization. A criterion based on both the values of the scaled residuals and the fulfilment of the global mass and energy balances is employed to judge the convergence. A simulation is converged when the values of the scaled residual are below $10^{-3}$ for mass and velocity and $10^{-6}$ for energy and turbulence, also when the mass and energy imbalances are less than 0.2%, and the continuous monitoring of certain flow variables does not show any change with successive iterations.

## 3. Experimental procedure

The simulations were validated by comparing the numerically predicted results with experimental measurements. Two different magnitudes were taken into consideration: the gas velocities and the gas mass flow rates. The gas consumptions were calculated from the pressure drop in the gas supply cylinder at a given time for a regulated atomisation pressure and the gas velocities were measured using the PIV technique. In order to corroborate some of the conclusions deduced from the simulations, some atomisations were also performed in the atomisation unit held at CEIT-BRTA research centre. In those experiments, the influence of the inlet gas pressure (P, varied from 20 to 60 bar) and the throat width of the gas nozzle ($0.6 \bullet L_o$ and $0.77 \bullet L_o$) on the resulting metal powders was investigated, using copper as the raw material and nitrogen as the atomising gas. A detailed explanation of the atomising procedure can be found in literature [49].

PIV technique was employed to compare the experimentally measured mean velocity fields with the results obtained computationally. Specifically, the velocity fields at four different gas inlet pressures were measured. The PIV does not directly measure the velocity of the fluid, but the dominant displacement of a group of particles. The flow is seeded with particles capable of reflecting the light and a double pulse laser light source is used to illuminate a cross section of the flow to be studied. A Charge-Coupled Device (CCD) camera is synchronized with the laser in order to capture one image per pulse of the laser light source. The acquired images are then processed and the displacements of the particles between a pair of images are measured (Fig. 4.a). Awareness of the time between the pulses of the laser light means that the gas velocities can be easily calculated (Fig. 4.b). The mean or time-average values of the velocity (Fig. 4.c) are obtained from a number of those instantaneous measurements [46,47].

It is not possible to employ the PIV technique inside the atomisation unit, so a dedicated test bench was built for this purpose. The setting up of the instruments is very important for both calibration and actual experiments (Fig. 5.a). The position of the laser light source and the CCD camera inside the test bench is shown in Fig. 5.b, where it is observed that both devices are located at the same level relative to the ground. The gas atomiser is assembled by a coupling fixture on a vertical column that allows displacements on the Z axis (vertical). In this way, the position of the gas atomiser can be adjusted in order to measure the mean velocity fields in areas closer to or further away from it. The installation of a gas supply line with a pressure regulator allows for the reproducing of gas flows typically used in real atomisations. During the calibration and measurement processes, the laser light sheet is aligned with a meridional plane of the gas atomiser (i.e. containing the central axis), while the CCD camera is positioned perpendicular to this plane in order to obtain a non-distorted measurement region. The distance between the camera and the measurement plane illuminated by the laser light sheet depends on the Field of View (FOV) considered.

The employed PIV system was designed and built by TSI Inc. The illumination source consists of a dual-head Nd-YAG Ultra PIV-120 laser manufactured by Big Sky Lasers Inc., which has a pulse energy of 120 mJ at a wavelength of 532 nm (green), a pulse frequency of 15 Hz and an exit beam diameter of 5.3 mm. The optics are mounted directly in front of the beam exit. The first component is a 15 mm cylindrical lens, which expands the circular beam onto a sheet with a thickness of approximately 1 mm. The second is a 500 mm spherical lens that focuses the sheet in such a way that the thinnest portion of the light sheet (waist) is located approximately at the centre of the measurement region. The images are captured by a CCD camera PowerView 4MP manufactured by TSI Inc., whose resolution is 2048 × 2048 pixels. The measurements are taken using a 105 mm focal length Nikon lens with a numerical aperture of 5.6. The seeding of the flow is produced by a commercial atomiser system model 9307 from TSI Inc., which uses a system of Lazkin nozzles to produce seed olive oil particles with a mean diameter of 1 μm and a standard deviation of 0.63 μm. The camera and laser are controlled by a synchronizer model 610035 with 1 ns of resolution. The calibration, data acquisition and processing processes are controlled and monitored using the Insight3G software. The calibration is performed using a calibration card placed accurately in the plane of the laser light sheet (measuring region) and taking an image of the card to relate the dimensions in pixels to real length dimensions.

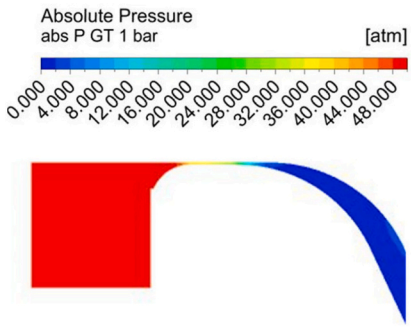


a) Expansion of the gas in the gas nozzle

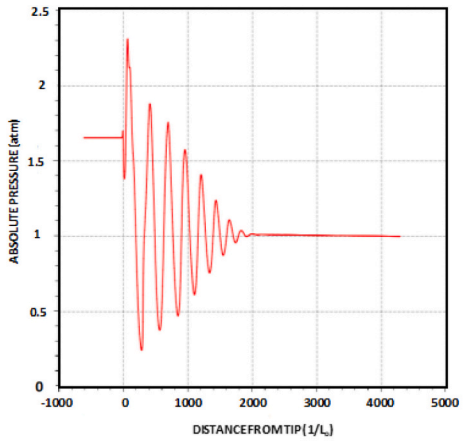


b) Static pressure in the symmetry axis

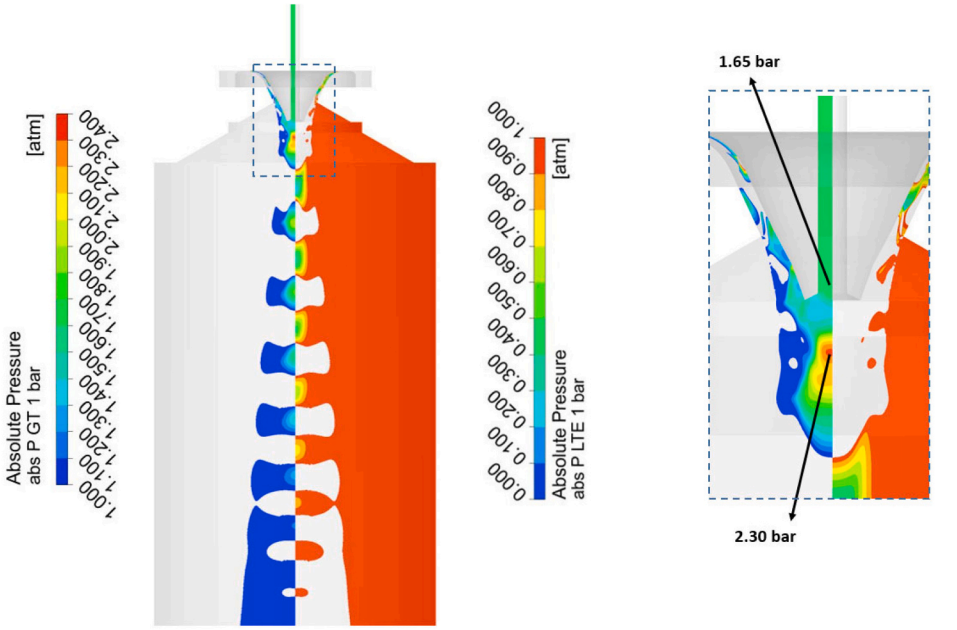


c) Regions of the domain with static pressure above the atmospheric pressure (left half) and below the atmospheric pressure (right half).

**Fig. 6.** Results related to the static pressure predicted by the simulation.

Correct processing of the captured images is essential to obtain the flow velocity fields. Each instantaneous measurement contains a pair of images, one for each laser pulse, separated by the time interval between laser pulses (Δt). The velocity field is found by dividing the images into small regions known as interrogation windows and performing a cross correlation between the pixel intensity of the images. A Gaussian fit with sub-pixel accuracy is used to find the correlation peak within each interrogation window. The image processing is based on a recursive algorithm executed in two steps [50]. In the first step, the cross-correlation on interrogation windows of 64 × 64 pixels is calculated and particle displacements are computed according to the selected Δt. The latter displacement is used in the second step with interrogation windows of 32 × 32 pixels. In this way, the number of particles in the inner interrogation area for the two images is maximized and a large number of valid vectors is obtained. Moreover, the recursive algorithm comprises of two processes for validating and conditioning the measurement. The validation process removes and replaces the spurious vectors through an interpolation procedure, in which it is necessary to control the Energy Level and the Peak to Noise Ratio . Subsequently, the conditioning process is used to smooth the velocity field.

The notable difference in velocity magnitudes hinders the use of a single FOV able to capture a domain of a similar size to the numerically simulated domain. This problem was circumvented by choosing two square overlapping FOVs of 55.4 mm, one on top of the other, except for the highest atomising pressure, where smaller FOVs of 41.4 mm were needed to resolve higher velocity values. A Δt between 500 and 900 ns

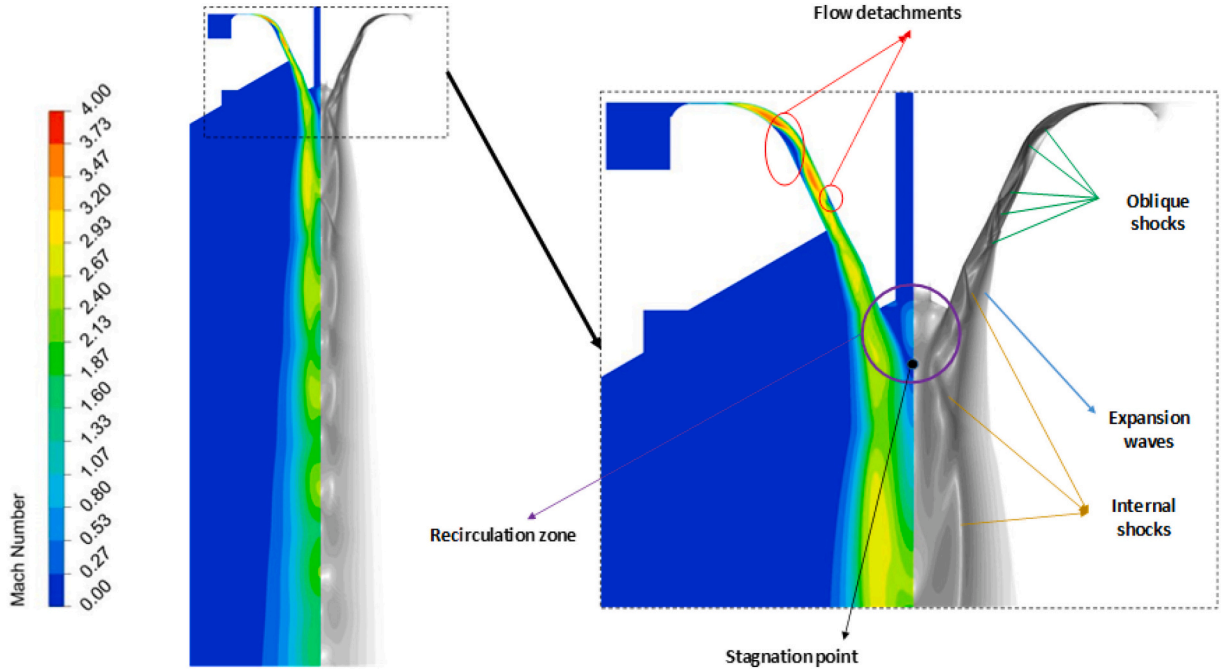


**Fig. 7.** Contours of local Mach number (left) and pseudo-Schlieren image (right), where singular characteristics of the gas flow dynamics are visible.

was selected according to the maximum displacement, which must be approximately 25% of the interrogation area [51]. In order to obtain a mean velocity field, the required number of image pairs increases with the turbulence of the flow. Thus, 500 pairs of images were taken for the upper region, closer to the gas atomiser, while this number was reduced to 250 for the lower region. Since the measurements were performed in the test bench instead of the atomisation unit and there was noexhaust line connected to the outside, nitrogen could not be used for security reasons. Therefore, compressed air was employed because its properties are quite similar to those of nitrogen.

## 4. Result and discussion

### 4.1. Simulation results

The computational simulations have revealed the main characteristics of the atomising gas flow in the absence of the melt stream. In this section, the results that explain the influence of both the gas inlet pressure and the throat length of the convergent-divergent gas nozzle are presented.

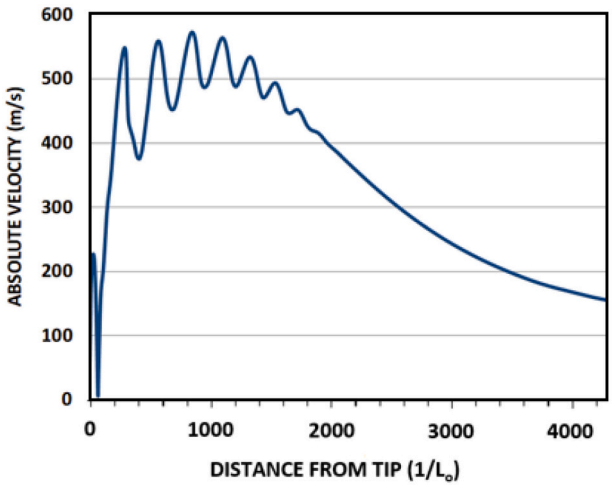


**Fig. 8.** Absolute velocity in the symmetry axis of the computational domain.

#### 4.1.1. Reference case

The simulation where nitrogen at 50 bar is modelled has been selected as the reference one to extract conclusions when analysing and comparing the results obtained with the different simulations. The throat of the gas nozzle in this simulation has a width of $L_o$. Under these conditions, the calculated nitrogen mass flow rate is 65 g/s.

The strong expansion of the gas passing through the supersonic nozzle is evident in Fig. 6.a, as it depressurizes abruptly from 50 bar at the inlet to the ambient pressure when it enters the atomisation chamber. In the throat, the static pressure is around 26 bar, which agrees with the value predicted by the one-dimensional equations for compressible isentropic flows [12,13]. Unlike convergent nozzles, which provide highly sub-expanded flows, convergent-divergent nozzles provide over-expanded or slightly under-expanded flows when the inlet pressure differs from the design pressure. Consequently, a series of expansion-compression waves are typically observed until the gas reaches the ambient pressure at a distance of 2140•$L_o$ from the melt tip, as seen plotted in Fig. 6.b. Fig. 6.c shows the regions of the atomisation chamber that have a static pressure lower (right half) or higher (left half) than the ambient pressure. The pressure field near the melt tip is very important. The idea of a good design of both the gas atomiser and the tip has always been linked to the achievement of suctions in this critical zone because it promotes the flow of the liquid metal from the crucible to the atomisation chamber, thus providing greater stability to the process. CEIT's atomisation unit allows the pressurization of the melting chamber up to 1.5 bar in order to push the melt when the suction level is very low or overpressures are detected. This reference simulation reveals that the calculated static pressure in the melt feed tube, which is also called aspiration pressure, is about 1.65 bar. As this value is higher than 1.5 bar, it will not be possible to perform experimental atomisations using nitrogen at 50 bar and a throat width $L_o$.

In contrast to the pressure, the velocity of the gas increases considerably as it passes through the gas atomiser. Fig. 7 reveals that the gas accelerates in the convergent part from very low subsonic velocities, reaches the sonic velocity at the throat and becomes supersonic in the divergent part. It is evident that the most effective zone for atomisation

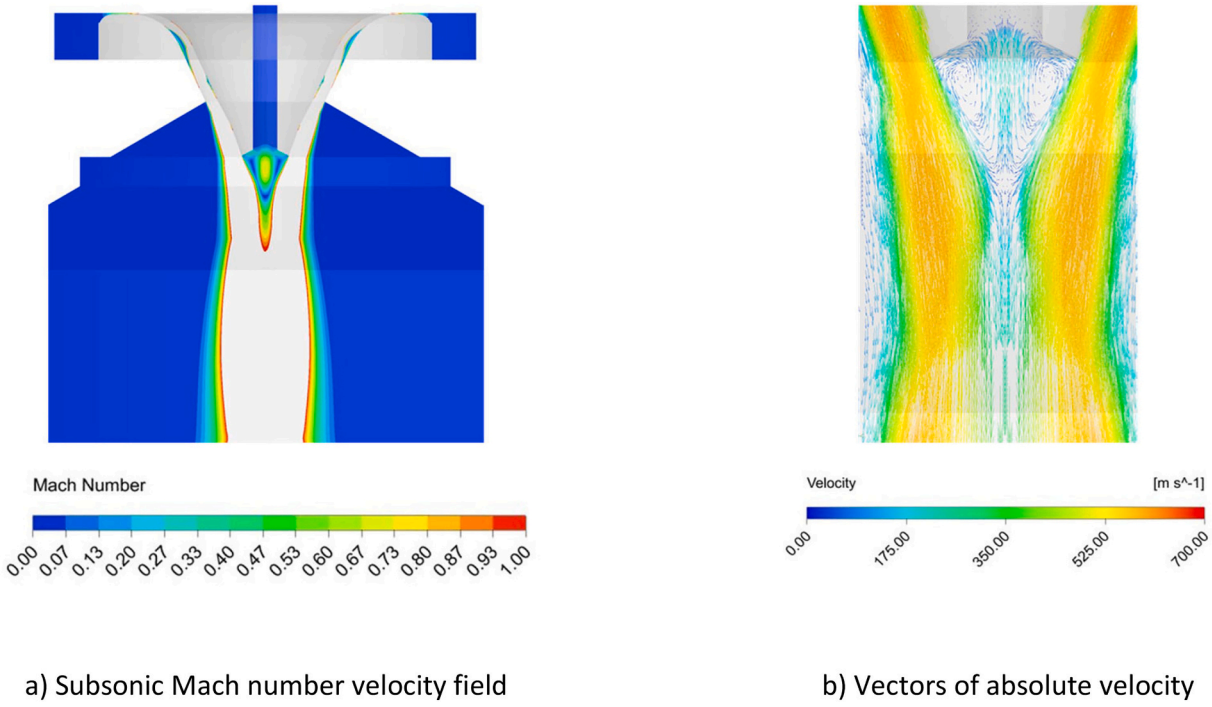


**Fig. 9.** Details of the recirculation zone.

is the central region of the atomisation unit, near the melt nozzle, where the highest velocities are attained. In the areas far from the axis, the gas velocity decreases drastically. Previous experimental and numerical studies have reported that the gas flow in close-coupled gas atomisation units exhibits a series of unique phenomena, such as oblique waves, expansion waves, recirculation zones, stagnation points and flow detachments [15–22]. All these characteristics are also present in this simulation, as shown in Fig. 7. As the high pressure gas enters the nozzle, the sharp angle with the nozzle causes a detachment of the flow. An oblique shock is subsequently formed inside the nozzle and is reflected by the outer surface. At the exit of the divergent part, the gas flow expands through a series of Prandtl-Meyer waves and recompression shocks to match the ambient pressure inside the atomisation chamber. Unlike the convergent nozzles, in which a Mach disc may also appear downstream due to the strong expansion of the gas, this kind of normal shock wave is never formed with the supersonic nozzles because of the lower intensity of the internal waves. A large amount of energy is dissipated as a result of these shock waves, so it would be beneficial to design a shock-free gas atomiser which would enhance the energy transfer from the atomising gas to the melt.

Fig. 8 shows the absolute velocity values obtained in the symmetry axis of the computational domain. The gas velocity inside the atomisation chamber is mainly composed of the axial component. A stagnation point (zero velocity point) is detected at a distance of around 57•$L_o$ from the melt tip, which corresponds to the maximum static pressure of Fig. 6.c.

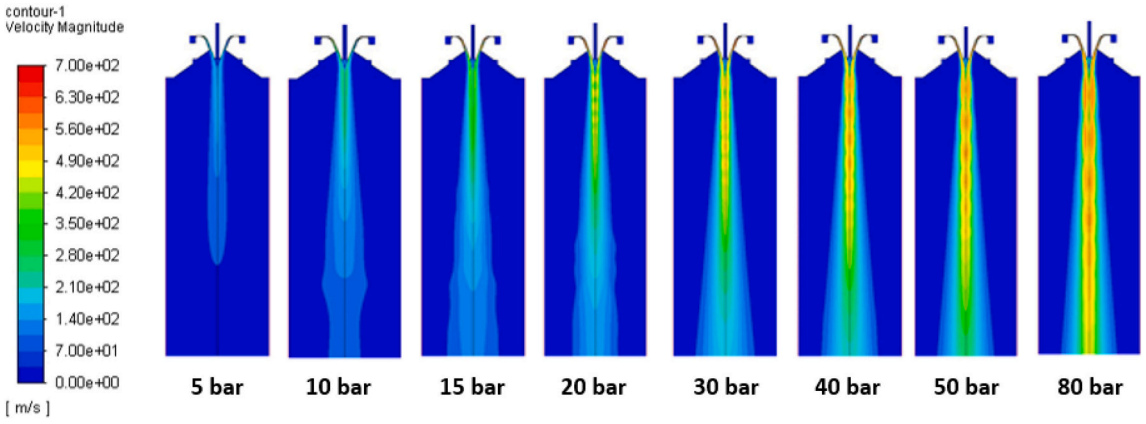


| | 5 bar | 10 bar | 15 bar | 20 bar | 30 bar | 40 bar | 50 bar | 80 bar |
|---|---|---|---|---|---|---|---|---|
| $m_g$ (g/s) | 5.9 | 12.2 | 18.7 | 25.4 | 38.3 | 51.5 | 52.3 | 105.7 |
| $P_{asp}$ (bar) | 1.01 | 1.07 | 1.07 | 1.08 | 1.15 | 1.39 | 1.65 | 1.70 |

**Fig. 10.** Absolute velocity fields at different Inlet pressures, indicating also the calculated Nitrogen mass flow rates and the aspiration pressures in the melt feed tube.

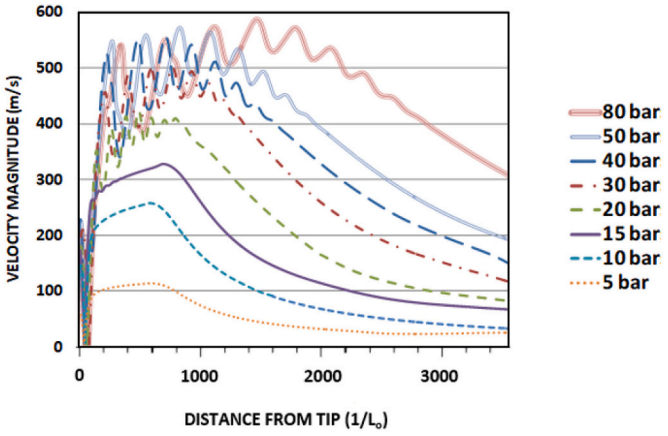


**Fig. 11.** Absolute velocity curves along the symmetry axis.

Fig. 9.a shows that the gas flow generates a recirculation zone or wake under the melt exit hole. The gas flow within this region is subsonic and is surrounded by an external gas flow with a much higher velocity. The velocities in this recirculation zone reach values higher than 200 m/s so they are not negligible. Although the length of the wake zone is usually small, in this case around 143•$L_o$, its influence on the atomisation process has been widely discussed over the years. The vector map of Fig. 9.b makes it possible to identify the direction of the gas flow in the wake and locate the stagnation point, where the gas velocity drops to zero and changes the flow direction. The absolute pressure at this point is high (around 2.3 bar). A good design of the components should ensure that this stagnation point is not extremely close to the tip exit, since its high pressure can prevent the correct flow of the melt from the tundish to the atomisation chamber. The figures show that the gas around the tip opposesthe flow of melt entering the atomisation chamber. The gas flow in the centre moves toward the melt feeding tube and turns outward in the radial direction when close to it. This fact causes the pre-filming of the liquid metal when it is atomised with close-coupled gas atomisers.

*4.1.2. Influence of the inlet pressure*

In this section, the results predicted by simulations with different inlet pressures are presented. As the gas flow dynamics have many similarities with the flow calculated in the reference case, only the most relevant observations are presented. The inlet pressure constitutes one of the main operational variables of the gas atomisation process, since it affects both the gas flow rate and its velocity. It is widely accepted that the experimental parameter that best correlates with the particle size distribution is the GMR ratio. Since higher values of this parameter provide finer powders, a refinement is more likely to be obtained if higher gas mass flow rates are employed [23,49,52–54]. In order to investigate the influence of the inlet gas pressure, a parametric study varying its value from 5 to 80 bar has been performed. Fig. 10 shows the nitrogen flow rates provided by eight different simulations, where it is observed that the nitrogen flow rate increases linearly with the inlet pressure.

The resulting velocity fields for the eight different inlet pressures are also shown in Fig. 10, while the absolute velocities on the symmetry axis are plotted in Fig. 11. The gas flow in the atomisation chamber passes from subsonic to supersonic at around 15 bar. It is also appreciated that the velocity gain is clearly non-linear with this operational variable: increasing the inlet pressure from 5 to 20 bar gives much higher velocity gains than when it is raised from 40 to 80 bar. Therefore, it can be stated that there is a point around 30 bar at which a systematic increase of the inlet pressure barely affects the velocity of the gas, confirming one of the conclusions of Aydin and Ünal [22]. These simulations also demonstrate that higher pressures are able to sustain a longer high velocity plume, so they enable the transfer of more kinetic energy to the melt, as reported in other studies [15,17].

The images in Fig. 12 show the evolution in size and shape of the wake formed below the tip for four simulations. Although its length remains practically constant, it is observed that the increase of the inlet pressure produces a progressive lateral reduction of the recirculation zone. This fact can be related to the gradual decrease of the melt flow rate observed experimentally when higher inlet pressures are used in experimental atomisations (see section 5.3). On the other hand, the simulations have only detected a very slight displacement of the stagnation point (i.e. the zero velocity point in the curves of Fig. 11), which indicates that the location of this point depends fundamentally on the geometry of the gas nozzle and the melt tip.

These simulations also provide the value of the aspiration pressure in the melt feed tube at different inlet pressures. None of them predict suctions that can promote the melt flow from the tundish to the atomisation chamber. Fig. 11 shows that the calculated aspiration pressures are slightly higher than the atmospheric pressure if an inlet pressure of less than 30 bar is imposed as the boundary condition. At higher inlet pressures, however, a sudden increase is clearly observed. Under these operational and geometric variables, particularly with a throat with $L_o$, it would only be possible to atomise if an inlet pressure below 40 bar is employed, since CEIT's atomisation unit only allows the pressurization of the melting chamber up to 1.5 bar.

*4.1.3. Influence of the throat width of the supersonic gas nozzle*

The geometry of the convergent-divergent nozzle influences the way in which the gas is accelerated during its expansion, and the throat width of the supersonic nozzle is considered as one of the most critical design parameters. In order to analyse the influence of this geometric

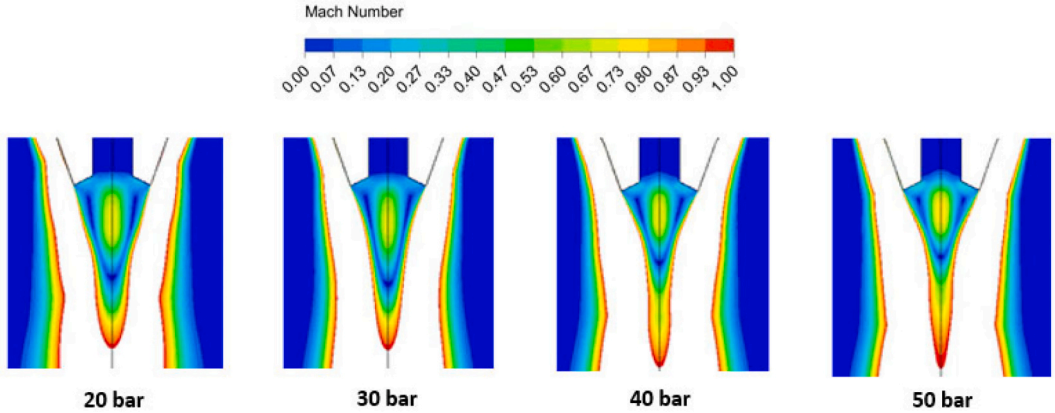


**Fig. 12.** Size and shape of the predicted recirculation zones.

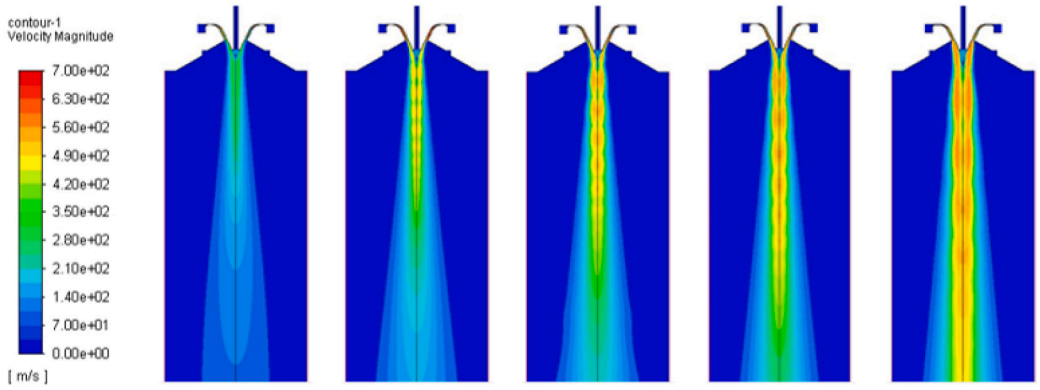


| | $0.29 \cdot L_o$ | $0.5 \cdot L_o$ | $0.77 \cdot L_o$ | $L_o$ | $2 \cdot L_o$ |
|---|---|---|---|---|---|
| $m_g$ (g/s) | 14.7 | 29.6 | 49.0 | 65.3 | 135.4 |
| $P_{asp}$ (bar) | 1.13 | 1.16 | 1.22 | 1.65 | 1.75 |

**Fig. 13.** Absolute velocity fields with different throat widths, indicating also the calculated Nitrogen mass flow rates and the aspiration pressures in the melt feed tube.

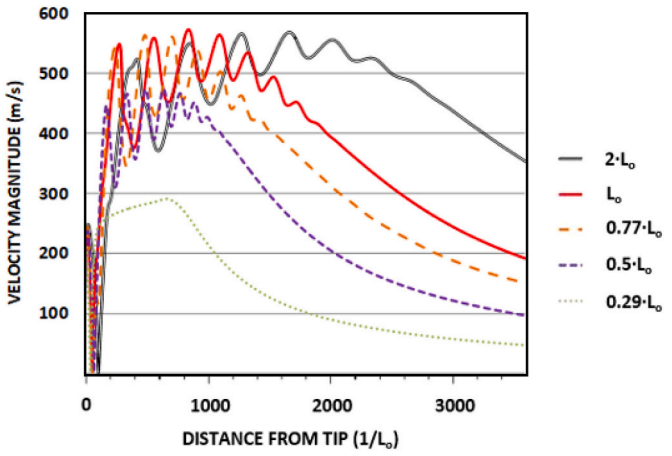


**Fig. 14.** Absolute velocity curves along the symmetry axis.

variable, four different simulations have been carried out, with throat widths of $0.29 \bullet L_o$, $0.5 \bullet L_o$, $0.77 \bullet L_o$ and $2 \bullet L_o$ and maintaining nitrogen at 50 bar as the atomising gas. The gas mass flow rates, absolute velocity fields, velocity curves along the symmetry axis and aspiration pressures in the melt feed tube predicted by the computational simulations are shown in Figs. 13 and 14. It can be stated that the increase in the throat width has a practically identical effect on the gas flow dynamics to the increase of the inlet gas pressure previously described, so the following conclusions can be listed:

- The nitrogen mass flow rates vary linearly with the throat width of the gas expansion nozzle (Fig. 13).
- If a smaller throat is simulated at a constant inlet pressure (50 bar), the obtained gas flow presents lower velocities in the atomisation chamber (Figs. 13 and 14). Depending on the throat width, subsonic or supersonic flows are predicted. Moreover, successive increases in the throat width provide a barely noticeable velocity gain once a supersonic flow has been achieved (Fig. 13). However, it is also observed that supersonic velocities are maintained at greater distances from the melt tip as this geometrical parameter is enlarged (Fig. 13).
- The calculated aspiration pressures in the melt feed tube are slightly higher than the atmospheric pressure with small throat widths, but higher overpressures are observed by increasing this geometric parameter (Fig. 13).

#### *4.1.4. Simultaneous treatment of the effect of both the inlet pressure and the throat width*

The similarities in the gas flow characteristics found when increasing the inlet pressure or the throat width of the gas nozzle can be conveniently unified, as shown in Fig. 15. The thick curve corresponds to the reference case, while the continuous and dashed lines show the effect of the inlet pressure and the throat width, respectively. The nitrogen mass flow rate predicted by each simulation is indicated next to each curve. It is observed that very similar atomisation conditions can be reproduced with different gas atomisers by properly adjusting the inlet pressure. For example, atomising at 40 bar using an atomiser with a throat width of $L_o$ gives almost identical gas mass flow rates and velocities as atomising at 50 bar using an atomiser with a throat width of $0.77 \bullet L_o$.

Another relevant conclusion drawn from Fig. 15 is that the gas mass flow rate and velocity vary proportionally, regardless of the inlet pressure and the throat width of the gas nozzle: the smaller the amount of gas introduced into the atomisation chamber, the lower its velocity and vice versa. Another example of this equivalence is shown in Fig. 16, where the aspiration pressures predicted by the simulations are plotted as a function of the gas mass flow rate. An overlap of the calculated overpressures on the same curve is observed. Consequently, in order to compare powders produced experimentally with different gas atomisers at different inlet pressures, the simplest option would be to correlate powder properties directly with the gas mass flow rate or velocity.

### *4.2. Experimental validation*

Experimental measurements of both the gas mass flow rate and velocity are compared with the results obtained computationally. The accuracy of the conclusions deduced from the numerical simulations is also evaluated by analysing the characteristics of some gas atomised powders.

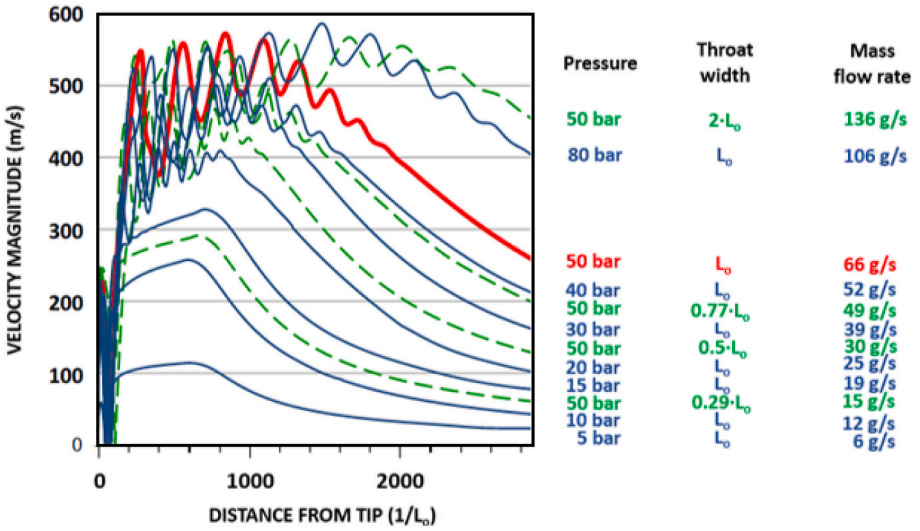


**Fig. 15.** Absolute velocity curves along the symmetry axis.

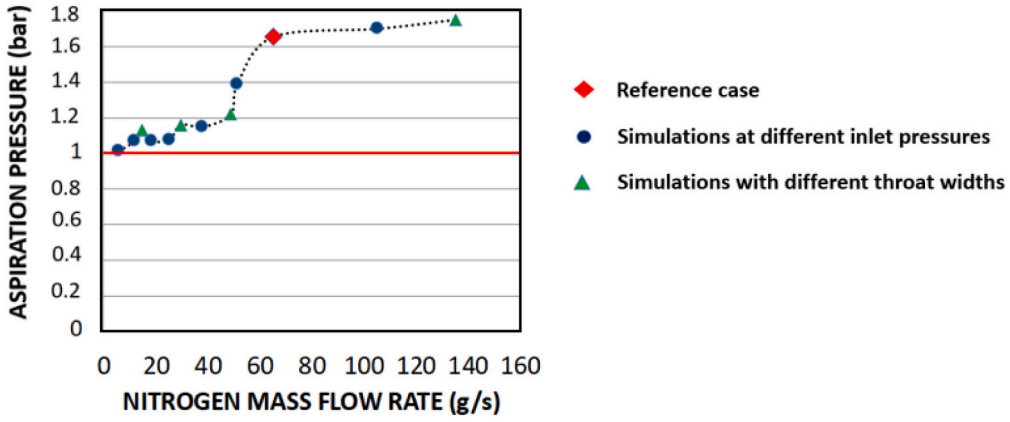


**Fig. 16.** Aspiration pressures as a function of the resulting gas mass flow rate.

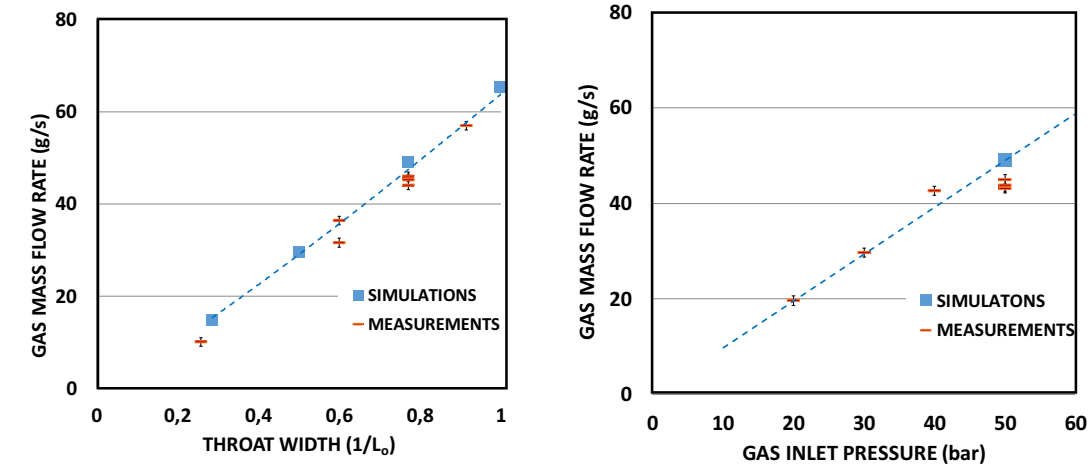


a) Gas atomisers with different throat widths at 50 bar

b) Different pressures using the gas atomiser with a throat width of 0.77·L$_o$

**Fig. 17.** Experimental and computational gas mass flow rates.

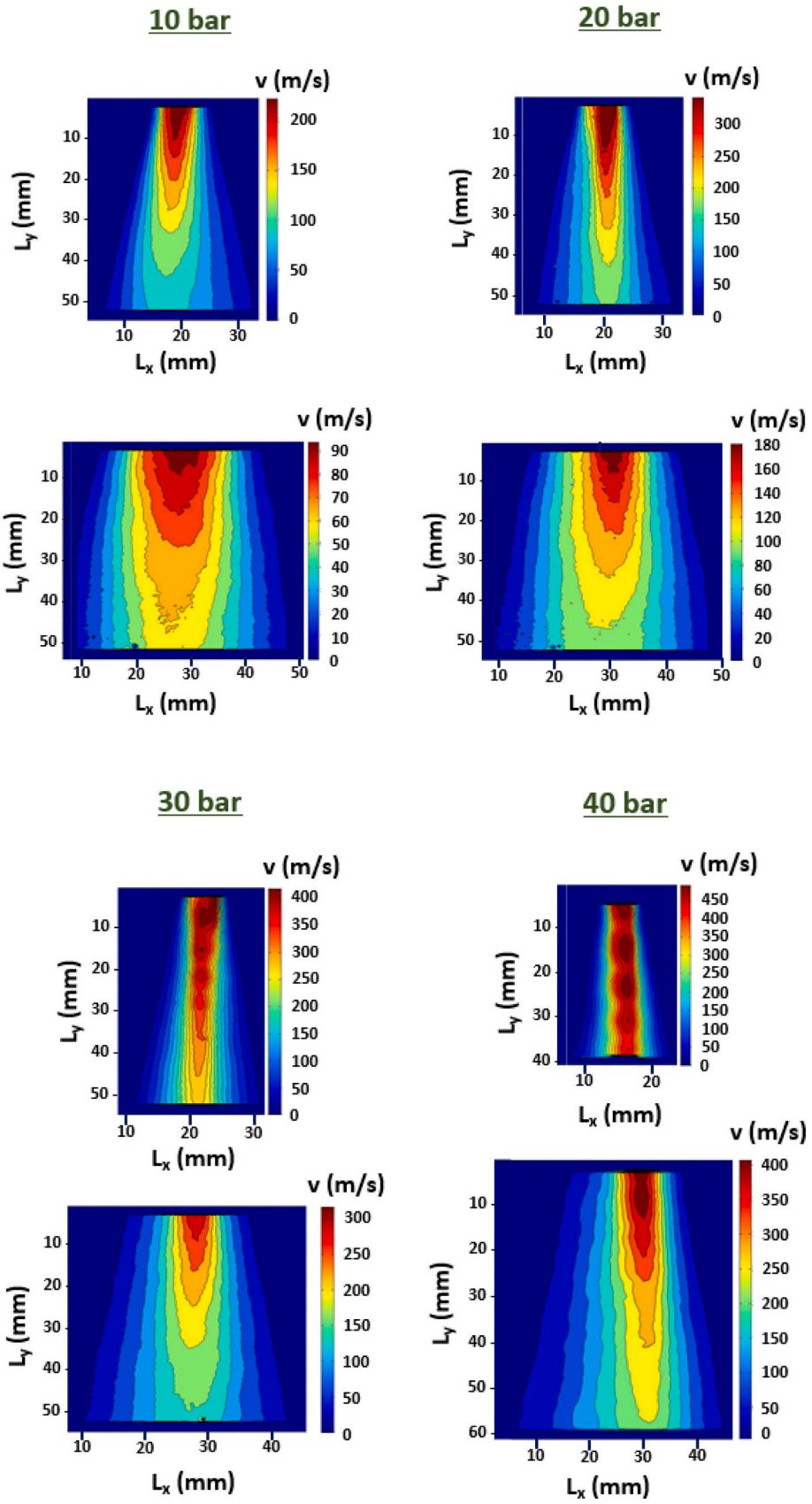


**Fig. 18.** Averaged absolute velocity fields measured in the region ranging from 3 to 8 cm below the melt tip at different inlet pressures of entrance.

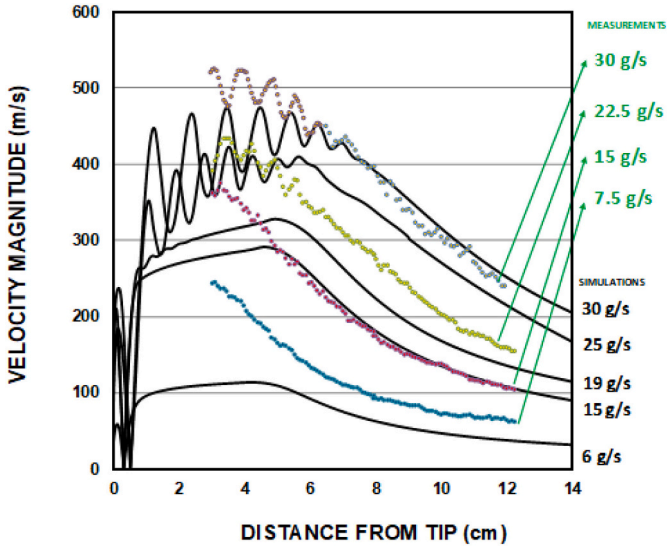


**Fig. 19.** Comparison between the measured and simulated velocities.

*4.2.1. Gas mass flow rates*

In order to demonstrate the validity of the gas consumptions predicted by simulations, the gas mass flow rates have been experimentally measured at different inlet pressures and using four atomisers with different throat widths (0.26•$L_o$, 0.6•$L_o$, 0.77•$L_o$ and 0.91•$L_o$).

The simulations varying the throat width of the supersonic gas nozzle were performed at 50 bar, so the experimental measurements with the different gas atomisers have also been conducted at that inlet pressure. The measured nitrogen mass flow rates are compared with the computational results in Fig. 17.a. There is a clear correlation between the simulations and the experimental data, with small differences that can be explained by the inherent error of flow measurement.

The effect of the inlet pressure has been studied by performing experimental measurements using the atomiser with a throat width of 0.77•$L_o$, whilst a throat width of $L_o$ was modelled in the simulations when the influence of this operational variable was analysed. Due to the complex geometry of the convergent-divergent nozzle, it was not possible to manufacture a nozzle with a throat width of exactly $L_o$. The difference in throat width between 0.77•$L_o$ and $L_o$ is less than 20 μm, which cannot be easily controlled using conventional machining procedures. However, this problem can be easily overcome as the simulations have shown that there is a perfect linear relationship between the inlet pressure and the resulting gas mass flow rate, and the gas consumption predicted with a throat width of 0.77•$L_o$ at a pressure of 50 bar is also known. From these two premises and using the simulation results obtained for $L_o$, the discontinuous line of Fig. 17.bwas constructed for a throat width of 0.77•$L_o$, which could be directly compared to the experimental measurements. A strong agreement between the simulations and the experimental data is observed again.

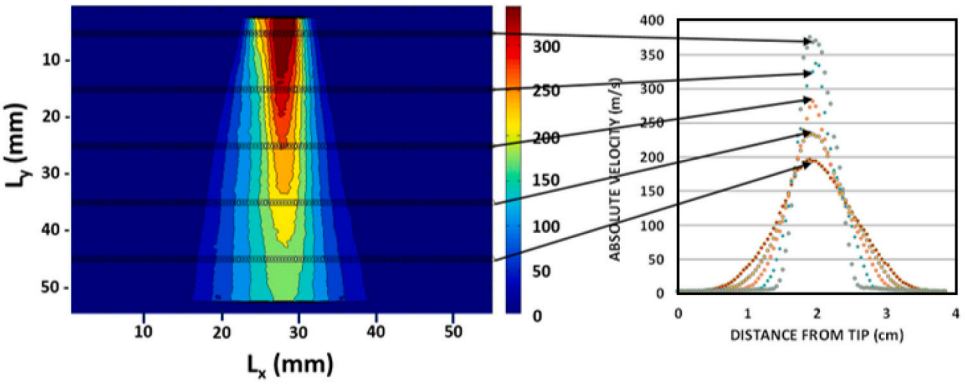


a) Region ranging from 3 to 8 cm below the melt tip

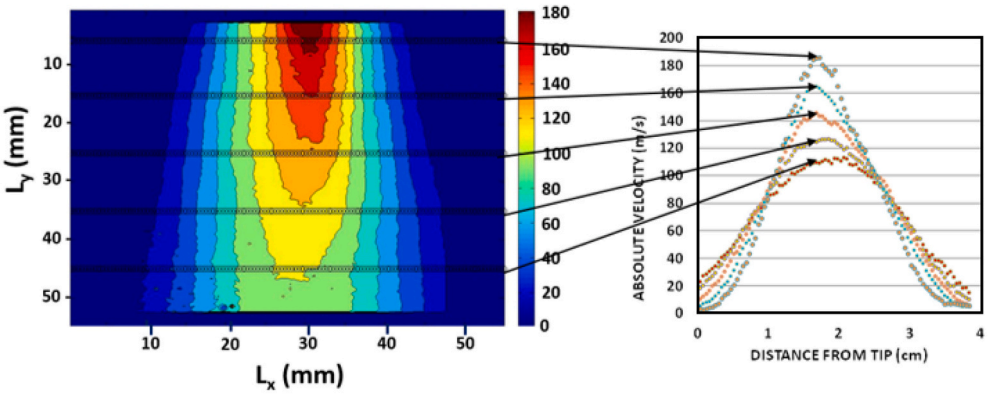


b) Region ranging from 7.5 to 12.5 cm below the melt tip

**Fig. 20.** Variation of the velocity along the radial direction when a gas mass glow rate of 15 g/s is regulated.

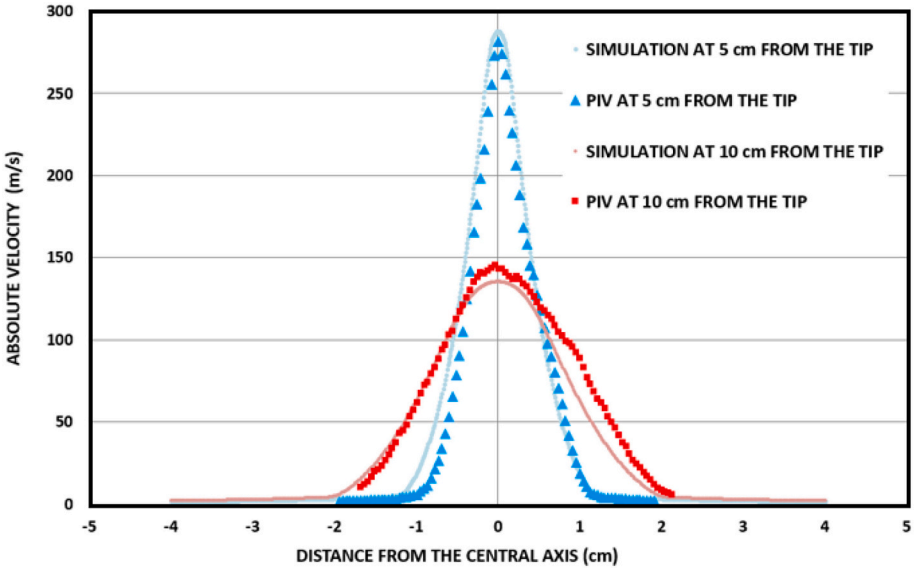


**Fig. 21.** Comparison between the experimentally measured and computationally predicted absolute velocities along radial direction at distances of 5 and 10 cm from the melt tip when a gas mass glow rate of 15 g/s is used.

*4.2.2. Gas velocities*

Fig. 18 shows the mean velocity field measured by the PIV technique for the atomiser with a throat width of 0.6•$L_o$ and inlet pressures of 10, 20, 30 and 40 bar on two overlapping regions of the spray area. These results are qualitatively similar to those calculated by the computational simulations:

a) The maximum velocity is reached at the centre of the gas jet and decreases downstream.
b) The gas flow assumes a predominantly conical shape.
c) There is a clear narrowing of the gas flow as the inlet pressure increases.
d) The flow is supersonic and expansion waves are observed above 30 bar, while the gas flow is subsonic and more uniform below 20 bar.

The experimental velocity magnitude in the centre of the two regions at different inlet pressures are plotted in Fig. 19, which illustrates the agreement that exists in the junction area of the curves measured between both regions. When the atomiser with a throat width of 0.6•$L_o$ is employed, inlet pressures of 10, 20, 30 and 40 bar give gas mass flow rates of approximately 7.5, 15, 22.5 and 30 g/s. If these gas velocity curves are plotted together with some of the velocity curves provided by the different simulations, it is corroborated that there is a close agreement between the experimentally measured values and those calculated computationally, mainly at distances greater than 5 cm from the melt nozzle (see Fig. 19). The differences in the zone closest to the tip may be due to the extreme difficulty in exactly aligning the measurement plane with the meridional plane of the atomiser.

The velocity fields predicted by the simulations and those obtained experimentally with the PIV technique have shown a broadening in the radial direction of the atomisation chamber. As explained previously, the shape of the gas jet is predominantly conical, so its width increases progressively with the distance from the tip. An example is shown in Fig. 20, where the velocity variations along the radial direction measured at five discrete heights for a gas mass flow rate of 15 g/s are plotted. The curves clearly show the progressive deceleration and widening of the gas when the axial distance from the melt nozzle is increased. In Fig. 21, the velocity variation along the radial direction at distances of 5 and 10 cm from the melt tip, obtained experimentally and numerically, are compared. As in the case of the absolute velocity curves along the axial direction, there is again a great similarity between the computational and experimental data.

*4.2.3. Experimental atomisations*

Table 1 provides a summary of the atomisations that have been performed with copper and nitrogen. The gas mass flow rate ($m_g$) is known from the results predicted by the simulations, whereas the average melt mass flow rate ($m_m$) has been calculated as the powder weight divided by the time length of each atomisation. The percentiles of 10th percent ($D_{10}$), 50th percent ($D_{50}$) and 90th percent ($D_{90}$) have

**Table 1**
Details of the experimental atomisation runs.

| Atomisation | Pressure (bar) | Throat width | $m_g$ (g/s) | $m_m$ (g/s) | GMR | $D_{10}$ (μm) | $D_{50}$ (μm) | $D_{90}$ (μm) |
|---|---|---|---|---|---|---|---|---|
| A | 30 | 0.6•$L_o$ | 22.76 | 37.5 | 0.61 | 20 | 67 | 216 |
| B | 30 | 0.6•$L_o$ | 22.76 | 48.0 | 0.48 | 28 | 74 | 234 |
| C | 40 | 0.6•$L_o$ | 30.35 | 23.8 | 1.27 | 17 | 44 | 104 |
| D | 40 | 0.6•$L_o$ | 30.35 | 39.0 | 0.78 | 12 | 53 | 166 |
| E | 50 | 0.6•$L_o$ | 37.94 | 21.7 | 1.75 | 7 | 33 | 95 |
| F | 50 | 0.6•$L_o$ | 37.94 | 22.5 | 1.68 | 8 | 40 | 145 |
| G | 60 | 0.6•$L_o$ | 45.53 | 13.8 | 3.3 | 4 | 23 | 62 |
| H | 60 | 0.6•$L_o$ | 45.53 | 14.8 | 3.08 | 4 | 22 | 57 |
| I | 20 | 0.77•$L_o$ | 19.62 | 48.4 | 0.41 | 28 | 77 | 211 |
| J | 30 | 0.77•$L_o$ | 29.42 | 45.5 | 0.65 | 19 | 55 | 141 |
| K | 40 | 0.77•$L_o$ | 39.23 | 49.3 | 0.81 | 16 | 45 | 140 |
| L | 50 | 0.77•$L_o$ | 49.04 | 22.9 | 2.14 | 8 | 28 | 72 |
| M | 50 | 0.77•$L_o$ | 49.04 | 17.2 | 2.86 | 7 | 26 | 65 |
| N | 50 | 0.77•$L_o$ | 49.04 | 9.30 | 5.27 | 5 | 21 | 53 |

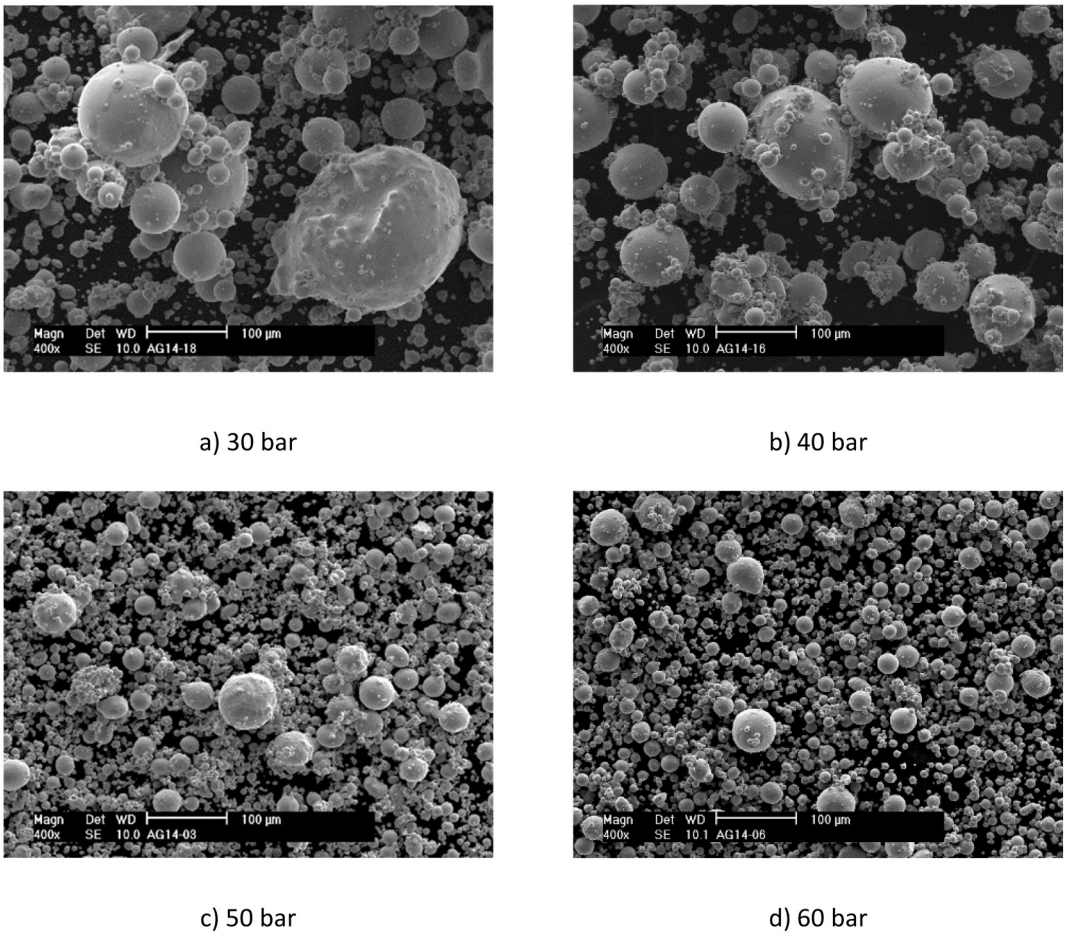


**Fig. 22.** Micrographs of powders produced with different pressures.

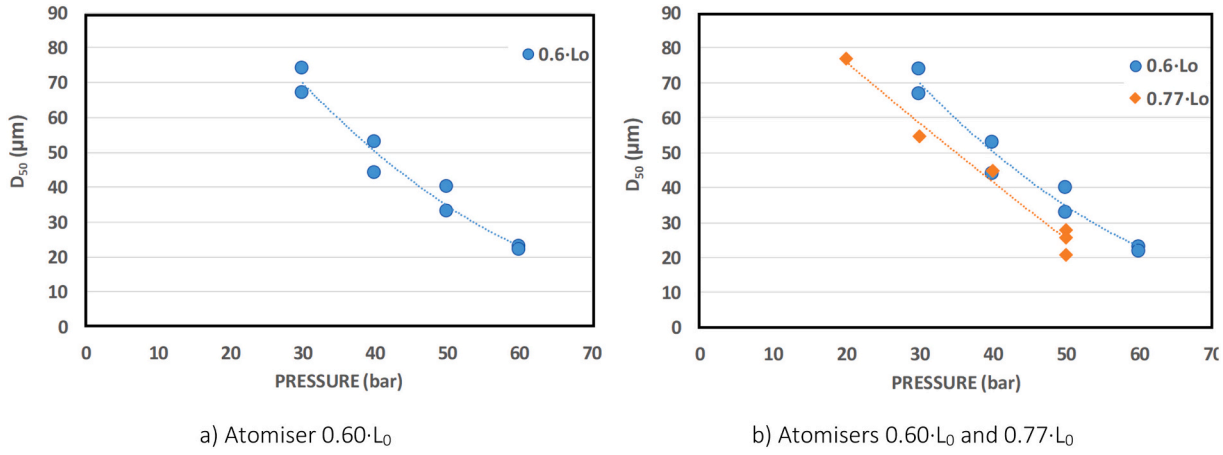


**Fig. 23.** Median particle size of the powders as a function of the inlet pressure.

been obtained from the measured particle size distributions of the different powders.

The effect of the gas inlet pressure on the particle size can be evaluated by analysing the data of the atomisations from A to H and the micrographs in Fig. 22. This operational variable strongly affects the particle size distribution of the atomised powders. Fig. 23.a demonstrates that a clear reduction of $D_{50}$ is obtained when the inlet gas pressure is raised, which is in agreement with the literature [55]. This fact is easily explained with the results predicted by the simulations: the use of a higher inlet pressure provides both higher velocities and a higher gas mass flow rate, so finer powders are produced. Fig. 23.b. compares the powders produced using the two atomisers with different throat widths. If the same inlet pressure is regulated, coarser powders are obtained with the $0.6 \bullet L_o$ atomiser because a lower gas mass flow rate and lower velocities are employed.

It has been stated before that the gas mass flow rate is a better parameter than the pressure to analyse metallic powders produced at different pressures and using different gas atomisers. Fig. 24.a shows

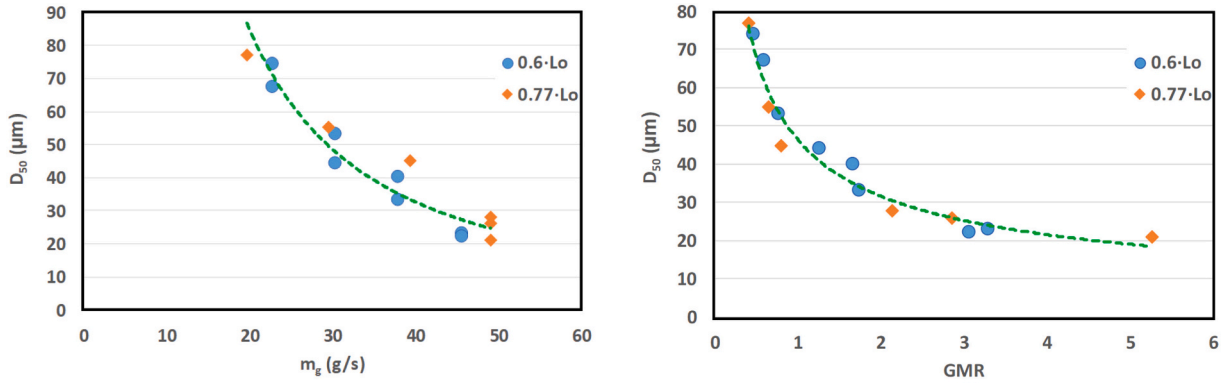


a) As a function of the gas mass flow rate

b) As a function of the GMR parameter

**Fig. 24.** Median particle size of the powders as a function of the gas mass flow rate and GMR parameter.

that a clear refinement of the atomised powders is observed when higher gas mass flow rates are employed. Additionally, Table 1 shows that melt flow rate decreases when the gas mass flow rate is increased. This trend can be qualitatively understood taking into account the simulation results of Fig. 12 and 16: when the gas mass flow rate is raised, there is a lateral reduction of the recirculation zone below the tip and the aspiration pressure in the melt feed tube goes up, which restricts the melt flow during real atomisations. The GMR parameter not only considers the gas mass flow rate, but also the melt mass flow rate. Consequently, it seems to be a better parameter to explain the trend of the particle size with the atomisation conditions. Fig. 24.b shows a much clearer correlation when this ratio is used to compare the particle size of different powders: higher GMR values produce finer powders.

## 5. Conclusions

CFD simulations that model the dynamics of the atomising gas flow provide valuable information about fundamental aspects of the gas atomisation process when the modelled geometries are realistic. The clear correlation between the numerical results and the experimental measurements of this study has confirmed that the CFD simulations are capable of correctly predicting the atomising gas flow dynamics inside the atomisation chamber. Therefore, they should be considered as a suitable tool for optimising the gas atomiser design in order to increase the efficiency of the gas atomisation process, thus obtaining powders with narrower particle size distributions. The following main conclusions can be drawn from the present study, focused on the influence of the inlet pressure and the throat width of a convergent-divergent gas nozzle:

- Increasing the inlet pressure or the throat area of the gas nozzle produces very similar effects on the gas flow: an increase in the gas mass flow rate, higher velocities in the atomisation chamber and longer supersonic plumes. Simulations have predicted the combined effect of both variables on the transition from subsonic to supersonic flows.
- The numerical results have highlighted that the throat width of the convergent-divergent gas nozzle has a strong influence in the gas flow characteristics. Due to the small dimensions of this geometric variable, which is below 100 µm, the gas atomiser is the most complex part to be machined within the indicated dimensional tolerances using conventional procedures. The results of this study have shown that a reduction of less than 20 µm in the throat width of the supersonic nozzle causes both a 26% of reduction in the resulting gas mass flow rate and 70 m/s less velocity if the same inlet pressure is modelled (see Fig. 15, 0.77•$L_o$ and $L_o$ gas atomisers at 50 bar). For this reason, it is essential to know the exact throat width of the gas nozzle that is going to be used to atomise in order to correctly adjust the atomising pressure. As previously explained, very similar atomisation conditions can be reproduced with different gas atomisers by properly adjusting the inlet pressure. For example, atomising at 40 bar using an atomiser with a throat width of $L_o$ gives almost identical gas mass flow rates and velocities as the atomiser with a throat width of 0.77•$L_o$ at 50 bar.
- The gas mass flow rate and the gas velocity are proportional regardless of the combination of operational and geometric variables: the smaller the amount of gas introduced into the atomisation chamber, the smaller its velocity and vice versa. Consequently, the resulting gas mass flow rate can be used as a single parameter to describe the combined effect of the inlet pressure and the throat width of the gas nozzle.
- The high pressure of the stagnation point can prevent the correct flow of the melt from the tundish to the atomisation chamber. The CFD simulations of this study have only detected a very slight displacement of this point when modelling different inlet pressures or gas atomisers. This fact indicates that its location depends fundamentally on the geometry of both the gas and the melt nozzles so a good design of these components should ensure that the stagnation point is not extremely close to the melt nozzle exit.
- Since there is a clear lack of experimental validation, the most important novelty of this study is related to the validation process followed after performing the CFD simulations. The agreement between the experimental measurements of gas mass flow rate and Particle Image Velocimetry (PIV) and the numerical results validates the CFD simulations as a tool to correctly predict the main characteristics of the atomising gas flow under different operational and geometric variables. The PIV technique had never previously been used for validation in the context of close-coupled gas atomisation process. This equipment has detected gas velocities very similar to those predicted by the simulations, with maximum differences in the order of 20 m/s in the central axis of the atomization chamber at distances greater than 5 cm from the melt nozzle. In addition, the PIV measurements in the radial direction have also confirmed that the simulations correctly predict the conicity of the gas jet.
- The atomised powders present different particle size distributions depending on the atomisation conditions, but they can be correctly explained using the data provided by the numerical results. As shown by the simulations, when the gas mass flow rate is raised, there is a lateral reduction of the recirculation zone below the tip and the aspiration pressure goes up. These two facts restrict the melt flow during real atomisations. As the Gas-to-Metal mass flow rate ratio (GMR) parameter not only considers the gas mass flow rate, but also the melt mass flow rate, it is shown that the GMR parameter exhibits

an excellent correlation with the particle size data of the produced powders.

## CRediT authorship contribution statement

**Ernesto Urionabarrenetxea:** Formal analysis, Investigation, Methodology, Validation, Visualization, Writing – original draft. **José Manuel Martín:** Conceptualization, Funding acquisition, Methodology, Supervision, Writing – review & editing. **Alejo Avello:** Formal analysis, Writing – review & editing. **Alejandro Rivas:** Conceptualization, Methodology, Writing – review & editing, Supervision.

## Declaration of Competing Interest

The authors declare that they have no known competing financial interests or personal relationships that could have appeared to influence the work reported in this paper.

## Acknowledgements

This work was supported by the Ministry of Economy, Industry and Competitiveness of the Spanish Government (grant number MAT2017-88957-R). Authors would also like to acknowledge the Spanish Ministry of Science and Innovation for the funding received for the CEFAM Project (grant number CER 20191005).

## Appendix A. Nomenclature tables

**Table A1**
Acronyms.

| | |
|---|---|
| AM | Additive Manufacturing |
| CCD | Charge-Coupled Device |
| CFD | Computational Fluid Dynamics |
| EVM | Eddy Viscosity Models |
| EL | Eulerian–Lagrangian |
| ELSA | Eulerian–Lagrangian Spray Atomisation |
| ESA | Eulerian Spray Atomisation |
| FOV | Field of View |
| GMR | Gas-to-melt mass flow rates Ratio |
| ICM | Interface Capturing Methods |
| LPT | Lagrangian Particle Tracking |
| PIV | Particle Image Velocimetry |
| FANS | Favre Averaged Navier Stokes |
| RS | Reynolds Stresses |

**Table A2**
Symbols.

| | |
|---|---|
| $c_v$ | Specific heat at constant volume |
| $c_p$ | Specific heat at constant pressure |
| $D_{10}$, $D_{50}$ and $D_{90}$ | The percentiles of 10th percent, 50th percent and 90th percent from the measured particle size distributions |
| $k$ | Turbulent Kinetic Energy |
| $L_o$ | Supersonic gas nozzle throat |
| $L_x$ and $L_y$ | Dimensions of the computational domain |
| $m_g$ | Gas mass flow rate |
| $m_m$ | Melt mass flow rate |
| $M_t$ | Turbulent Mach number |
| $p$ | Pressure |
| $Pr_t$ | Turbulent Prandtl number |
| $R = \Lambda/M_w$ | $\Lambda$ Ideal gas constant<br>$M_w$ Molecular weight |
| $S_{ij}$ | Mean strain rate tensor |
| $T$ | Temperature |
| $t$ | Time |
| $t_{ij}$ | Compact notation for the viscous stress tensor |
| $u_i$ | Components of the velocity vector in the $x_i$ directions |
| $x_i$ | Directions |
| $\widetilde{\varphi}$ or $\overline{\varphi}$ | Favre or Reynolds average |
| $\varphi''$ | Fluctuating value of the flow variable |
| $\Delta t$ | Time interval between laser pulses |
| $\delta_{ij}$ | Kronecker delta |
| $\varepsilon$ | Dissipation Rate of Turbulent Kinetic Energy |
| $\eta$ | Ratio between the turbulence and average flow time scales |
| $\lambda$ | Thermal conductivity |
| $\lambda_t$ | Turbulent thermal conductivity |
| $\mu$ | Dynamic viscosity |
| $\mu_t$ | Turbulent viscosity |
| $\rho$ | Density |
| $\tau_{ij}$ | Compact notation for the Reynold Stresses |
| $\Omega_{ij}$ | Rate-of-rotation tensor |
| $\vartheta$ | Velocity characteristic scale |
| $\ell$ | Length characteristic scale |
| $A_0$, $A_S$,$\phi$, $W$, $U^*$, $C_\mu$, $\sigma_k$, $\sigma_\varepsilon$, $C_1$, $C_2$ | Realizable k- $\varepsilon$ turbulence model parameters |

## Appendix B. Governing equations and turbulence model [56]

The Navier-Stokes equations govern the flow of any fluid. For compressible gases as an atomising gas, it is necessary to solve the equations of conservation of mass (1), conservation of momentum (2) and conservation of energy (3). Moreover, an equation of the state of thermodynamic equilibrium that relates the variables of pressure ($p$), density ($\rho$) and temperature ($T$) must also beconsidered in order to obtain a closed system of equations. In this study, the atomization gas has been considered as an ideal gas, so the ideal gas law (4) has been used.

$$\frac{\partial \rho}{\partial t}+\frac{\partial}{\partial x_i}(\rho u_i)=0 \tag{1}$$

$$\frac{\partial}{\partial t}(\rho u_i)+\frac{\partial}{\partial x_j}\left(\rho u_j u_i\right)=-\frac{\partial p}{\partial x_i}+\frac{\partial t_{ij}}{\partial x_j} \tag{2}$$

$$\frac{\partial}{\partial t}\left[\rho\left(c_v T+\frac{1}{2}u_i u_i\right)\right]+\frac{\partial}{\partial x_j}\left[\rho u_j\left(c_p T+\frac{1}{2}u_i u_i\right)\right]=\frac{\partial}{\partial x_j}\left(u_i t_{ij}\right)+\frac{\partial}{\partial x_j}\left(\lambda\frac{\partial T}{\partial x_j}\right) \tag{3}$$

$$p=\rho R T \tag{4}$$

where $u_i$ are the components of the velocity vector in the $x_i$ directions, $t$ is time, $\lambda$ is thermal conductivity, $R$ is the ideal gas constant, and $c_v$ and $c_p$ are respectively the specific heat at constant volume and pressure. The compact notation for the viscous stress tensor $t_{ij}$, according to the Stokes hypothesis, is:

$$t_{ij}=2\mu s_{ij}-\left(\frac{2\mu}{3}\right)\frac{\partial u_k}{\partial x_k}\delta_{ij} \tag{5}$$

where $\delta_{ij}$ is the Kronecker's delta, $\mu$ is the dynamic viscosity and $s_{ij}$ is the strain rate tensor.

$$s_{ij}=\frac{1}{2}\left(\frac{\partial u_i}{\partial x_j}+\frac{\partial u_j}{\partial x_i}\right) \tag{6}$$

Closed solutions of the Navier-Stokes equations can only be obtained for a few flows in simple geometries and in a laminar flow regime. For this reason, there is no choice but to solve the aforementioned equations numerically when studying complex flows. *Computational Fluid Mechanics* allows the simulation of turbulent flows to be approached from a statistical point of view, guiding it to calculate only the averaged characteristics of the flow. The basic concept is the decomposition of the flow variables ($\varphi$) into an average value ($\widetilde{\varphi}$) and into a fluctuating value ($\varphi''$) due to turbulence. For compressible turbulent flows that decomposition is obtain through Favre averaging:

$$\overline{\rho\varphi}=\overline{\rho}\widetilde{\varphi} \tag{7}$$

where overbar denotes Reynolds average.

The group of equations that govern the turbulent flow of compressible fluids are the Favre Averaged Navier-Stokes (FANS) Eqs. (7–9):

$$\frac{\partial \overline{\rho}}{\partial t}+\frac{\partial}{\partial x_i}(\overline{\rho}\widetilde{u}_i)=0 \tag{8}$$

$$\frac{\partial}{\partial t}(\overline{\rho}\widetilde{u}_i)+\frac{\partial}{\partial x_i}\left(\overline{\rho}\widetilde{u}_i\widetilde{u}_j\right)=-\frac{\partial \overline{p}}{\partial x_i}+\frac{\partial}{\partial x_j}\left(\bar{t}_{ij}-\overline{\rho u_i'' u_j''}\right) \tag{9}$$

$$\frac{\partial}{\partial t}\left[\overline{\rho}\left(c_v\widetilde{T}+\frac{1}{2}\widetilde{u}_i\widetilde{u}_i\right)+\frac{1}{2}\overline{\rho u_i'' u_i''}\right]+\frac{\partial}{\partial x_j}\left[\overline{\rho}\widetilde{u}_j\left(c_p\widetilde{T}+\frac{1}{2}\widetilde{u}_i\widetilde{u}_i\right)+\widetilde{u}_j\frac{\overline{\rho u_i'' u_i''}}{2}\right]=$$

$$\frac{\partial}{\partial x_j}\left[\widetilde{u}_i\left(\bar{t}_{ij}-\overline{\rho u_i'' u_j''}\right)\right]+\frac{\partial}{\partial x_j}\left(\lambda\frac{\partial\widetilde{T}}{\partial x_j}-c_p\overline{\rho u_j'' T''}+\overline{u_i'' t_{ij}}-\frac{\overline{\rho u_j'' u_i'' u_i''}}{2}\right) \tag{10}$$

$$\overline{p}=\overline{\rho}R\widetilde{T} \tag{11}$$

The effect of the fluctuations of the variables on the average flow is represented by terms defined by statistical correlations between the fluctuating values. The terms ($\overline{\rho}\tau_{ij}=-\overline{\rho u_i'' u_j''}$) are called Reynolds Stresses (RS). In total, there are six different tensions due to the symmetry of the RS tensor. Similarly, in the temperature transport Eq. (10) another three new terms appear due to products between velocities and fluctuating temperatures $\left(-c_p\overline{\rho u_j'' T''}\right)$. Therefore, it is essential to add nine additional equations to be able to close the system formed by the FANS equations. This circumstance is known as the Turbulence Closure Problem and makes the introduction of physical models essential. The most widely used turbulence models in industry are the Eddy Viscosity Models (EVM), which model the nine terms directly with the average strain rates and with the gradient of the average temperature value.

In this study, the Realizable $k-\varepsilon$ model has been used, which introduces two extra transport equations. Based on the Boussinesq hypothesis, it assumes that the RS are proportional to the average velocity gradients through the same turbulent viscosity magnitude $\mu_t$ for each of the components:

$$\overline{\rho u_i'' u_j''}=2\mu_t\left[S_{ij}-\left(\frac{1}{3}\right)\frac{\partial\widetilde{u}_k}{\partial x_k}\delta_{ij}\right]-\frac{2}{3}\overline{\rho}k\delta_{ij} \tag{12}$$

where $k$ is the Turbulent Kinetic Energy and $S_{ij}$ the mean strain rate tensor, which are defined as:

$$\overline{\rho}k = \frac{1}{2}\overline{\rho u_i^{''} u_i^{''}} \tag{13}$$

$$S_{ij} = \frac{1}{2}\left(\frac{\partial \widetilde{u}_i}{\partial x_j} + \frac{\partial \widetilde{u}_j}{\partial x_i}\right) \tag{14}$$

On the other hand, the terms $\left(-c_p\overline{\rho u_j^{''} T^{''}}\right)$ are modeled in a similar way to the RS, assuming that they are proportional to the gradient of the average value of the temperature through another magnitude $\lambda_t$ called turbulent thermal conductivity:

$$-c_p\overline{\rho u_j^{''} T^{''}} = \lambda_t \frac{\partial \overline{\overline{T}}}{\partial x_i} \tag{15}$$

The Reynolds' analogy stablishes a relationship between $\lambda_t$ and $\mu_t$ through the Prandtl number $Pr_t$, which is usually considered constant and the value 0.9 is adopted.

$$\lambda_t = \frac{c_p \mu_t}{Pr_t} \tag{16}$$

Therefore, calculating the turbulent viscosity $\mu_t$ adequately is the fundamental objective of the Realizable $k-\varepsilon$ turbulence model. From a purely dimensional perspective, it can be deduced that $\mu_t$ can be calculated as the product of the density of the fluid and the velocity ($\vartheta$) and length ($\ell$) characteristic scales of the turbulence:

$$\mu_t = C\overline{\rho}\vartheta\ell \tag{17}$$

The Realizable $k-\varepsilon$ model uses the statistical magnitudes Turbulent Kinetic Energy ($k$, $\left[\frac{L^2}{T^2}\right]$) and Dissipation Rate of Turbulent Kinetic Energy ($\varepsilon$, $\left[\frac{L^2}{T^3}\right]$) to determine the turbulence scales mentioned above. Considering the dimensions of these magnitudes, the turbulent viscosity can be calculated as follows:

$$\mu_t = \overline{\rho} C_\mu \frac{k^2}{\varepsilon} \tag{18}$$

where:

$$\overline{\rho}\varepsilon = \overline{t_{ij}\frac{\partial u_i^{''}}{\partial x_j}} \tag{19}$$

In this model, the coefficient $C_\mu$ is calculated as a function of the mean strain rate ($S_{ij}$) and rate-of-rotation ($\Omega_{ij} = \frac{1}{2}\left(\frac{\partial \widetilde{u}_i}{\partial x_j} + \frac{\partial \widetilde{u}_j}{\partial x_i}\right)$) tensors of the form:

$$C_\mu = \frac{1}{A_0 + A_S U^* \frac{k}{\varepsilon}} \tag{20}$$

where

$$U^* = \sqrt{S_{ij}S_{ij} + \Omega_{ij}\Omega_{ij}} \tag{21}$$

$$A_0 = 4.04 \tag{22}$$

$$A_S = \sqrt{6}\, cos\phi \tag{23}$$

$$\phi = \frac{1}{3} cos^{-1}\left(\sqrt{6}\, W\right) \tag{24}$$

$$W = \frac{S_{ij}S_{jk}S_{ki}}{\left(S_{ij}S_{ij}\right)^{\frac{3}{2}}} \tag{25}$$

The modeled transport equation of $k$ is obtained by a mathematical development of its exact transport equation, while the modeled transport equation of ε is obtained from the exact transport equation of the root mean square of the vorticity fluctuations.

$$\frac{\partial}{\partial t}\left(\overline{\rho}k\right) + \frac{\partial}{\partial x_j}\left(\overline{\rho}k\widetilde{u}_j\right) = \frac{\partial}{\partial x_j}\left[\left(\mu + \frac{\mu_t}{\sigma_k}\right)\frac{\partial k}{\partial x_j}\right] + 2\mu_t S_{ij}S_{ij} - \overline{\rho}\varepsilon - 2\overline{\rho}\varepsilon M_t^2 \tag{26}$$

$$\frac{\partial}{\partial t}\left(\overline{\rho}\varepsilon\right) + \frac{\partial}{\partial x_j}\left(\overline{\rho}\varepsilon\widetilde{u}_j\right) = \frac{\partial}{\partial x_j}\left[\left(\mu + \frac{\mu_t}{\sigma_\varepsilon}\right)\frac{\partial \varepsilon}{\partial x_j}\right] + \overline{\rho}C_{\varepsilon 1}\sqrt{2S_{ij}S_{ij}}\varepsilon - \overline{\rho}C_{\varepsilon 2}\frac{\varepsilon^2}{k + \sqrt{\frac{\mu}{\overline{\rho}}\varepsilon}} \tag{27}$$

where turbulent Mach number $M_t$ are defined by the following expression:

$$M_t = \sqrt{\frac{k}{a^2}} = \sqrt{\frac{k}{\frac{c_p}{c_v}R\widetilde{T}}} \tag{28}$$

and being the constants $\sigma_k = 1$ (21); $\sigma_\varepsilon = 1.2$ (22); $C_{\epsilon 2} = 1.9$ (23) and $C_{\epsilon 1} = max\left[0.43, \frac{\eta}{\eta+5}\right]$ (24), where $\eta$ can be considered the ratio between the turbulence and average flow time scales:

$$\eta = S\frac{k}{\varepsilon} \tag{29}$$

## References


[1] A.J. Yule, J.J. Dunkley, Atomisation of Melts, Oxford University Press, 1994.
[2] R.M. German, Powder Metallurgy and Particulate Materials Processing: The Processes, Materials, Products, Properties and Applications, Met. Powder Ind. Fed. (MPIF), Princeton, NJ,USA, 2005.
[3] A. Lawley, Atomization: The Production of Metal Powders, 2005.
[4] A. Amatriain, E. Urionabarrenetxea, A. Avello, J.M. Martín, Multiphase model to predict particle size distributions in close-coupled gas atomization, Int. J. Multiphase Flow 154 (2022), 104138, https://doi.org/10.1016/j.ijmultiphaseflow.2022.104138.
[5] M.Z. Gao, B. Ludwig, T.A. Palmer, Impact of atomization gas on characteristics of austenitic stainless steel powder feedstocks for additive manufacturing, Powder Technol. 383 (2021) 30–42, https://doi.org/10.1016/j.powtec.2020.12.005.
[6] S. Cooke, K. Ahmadi, S. Willerth, R. Herring, Metal additive manufacturing: technology, metallurgy and modelling, J. Manuf. Process. 57 (2020) 978–1003, https://doi.org/10.1016/j.jmapro.2020.07.025.
[7] X. Gang Li, Q. Zhu, S. Shu, J. Zhong Fan, S. Ming Zhang, Fine spherical powder production during gas atomization of pressurized melts through melt nozzles with a small inner diameter, Powder Technol. 356 (2019) 759–768, https://doi.org/10.1016/j.powtec.2019.09.023.
[8] K.L. Alvarez, H.A. Baghbaderani, J.M. Martín, N. Burgos, M. Ipatov, Z. Pavlovic, P. McCloskey, A. Masood, J. Gonzalez, Novel Fe-based amorphous and nanocrystalline powder cores for high-frequency power conversion, J. Magn. Magn. Mater. 501 (2020), https://doi.org/10.1016/j.jmmm.2020.166457.
[9] V.R. Faradonbeh, S. Rabiei, H. Rabiei, M. Goodarzi, M.R. Safaei, C.X. Lin, Power-law fluid micromixing enhancement using surface acoustic waves, J. Mol. Liq. 347 (2022), 117978, https://doi.org/10.1016/j.molliq.2021.117978.
[10] S.H. Delbari, A. Nejat, M.H. Ahmadi, A. Khaleghi, M. Goodarzi, Numerical modeling of aeroacoustic characteristics of different savonius blade profiles, Int. J. Numer. Methods Heat Fluid Flow 30 (2020) 3349–3369, https://doi.org/10.1108/HFF-12-2018-0764.
[11] M.N.H. Mat, N.Z. Asmuin, M.F.M. Basir, M. Goodarzi, M.F.A. Rahman, R. Khairulfuaad, B.A. Jabbar, M.S.M. Kasihmuddin, Influence of divergent length on the gas-particle flow in dual hose dry ice blasting nozzle geometry, Powder Technol. 364 (2020) 152–158, https://doi.org/10.1016/j.powtec.2020.01.060.
[12] M.N.H. Mat, N.Z. Asmuin, M.F. Md Basir, T. Abbas, M.S. Mohd Kasihmuddin, M. Goodarzi, Influence of nozzle area ratio on the gas-particle flow for single-hose dry ice blasting nozzle, J. Therm. Anal. Calorim. 143 (2021) 2343–2354, https://doi.org/10.1007/s10973-020-09714-8.
[13] M.N.H. Mat, N.Z. Asmuin, M.F. Md Basir, M.R. Safaei, M.S. Mohd Kasihmuddin, T. K. Ahmad Khairuddin, M. Godarzi, Optimizing nozzle convergent angle using central composite design on the particle velocity and acoustic power level for single-hose dry ice blasting nozzle, J. Therm. Anal. Calorim. 144 (2021) 2159–2173, https://doi.org/10.1007/s10973-020-10083-5.
[14] M.N.H. Mat, N. Asmuin, M.F. Md Basir, M.A. Alazwari, M.R. Safaei, Aeroacoustic analysis of dry ice blasting on divergent nozzle length using CFD to acoustic couple simulation, J. Therm. Anal. Calorim. 147 (2022) 6437–6448, https://doi.org/10.1007/s10973-021-10931-y.
[15] J. Mi, R.S. Figliola, I.E. Anderson, A numerical simulation of gas flow field effects on high pressure gas atomization due to operating pressure variation, Mater. Sci. Eng. A 208 (1996) 20–29, https://doi.org/10.1016/0921-5093(95)10046-6.
[16] M.P. Planche, O. Khatim, L. Dembinski, C. Coddet, L. Girardot, Y. Bailly, Velocities of copper droplets in the De Laval atomization process, Powder Technol. 229 (2012) 191–198, https://doi.org/10.1016/j.powtec.2012.06.031.
[17] S.P. Mates, S.D. Ridder, F.S. Biancaniello, R.W. Christinsen, Comparison of the supersonic length and dynamic pressure characteristics of discrete-jet and annular close-coupled nozzles used to produce fine metal powders, in: Proc. TMS Annu. Meet, 2000, pp. 71–81. Tennessee, USA, http://www.nist.gov/manuscript-publication-search.cfm?pub_id=852951.
[18] J. Ting, I.E. Anderson, A computational fluid dynamics (CFD) investigation of the wake closure phenomenon, Mater. Sci. Eng. A 379 (2004) 264–276, https://doi.org/10.1016/j.msea.2004.02.065.
[19] N. Zeoli, S. Gu, Computational validation of an isentropic plug nozzle design for gas atomisation, Comput. Mater. Sci. 42 (2008) 245–258. http://linkinghub.elsevier.com/retrieve/pii/S0927025607002005 (accessed May 6, 2013).
[20] Z. Li, G. Zhang, Z. Li, Y. Zhang, W. Xu, Simulation of gas flow field in Laval nozzle and straight nozzle for powder metallurgy and spray forming, J. Iron Steel Res. Int. 15 (2008) 44–47, https://doi.org/10.1016/S1006-706X(08)60264-2.
[21] A. Allimant, M.P. Planche, Y. Bailly, L. Dembinski, C. Coddet, Progress in gas atomization of liquid metals by means of a De Laval nozzle, Powder Technol. 190 (2009) 79–83. http://linkinghub.elsevier.com/retrieve/pii/S0032591008002246 (accessed April 10, 2013).
[22] O. Aydin, R. Unal, Experimental and numerical modeling of the gas atomization nozzle for gas flow behavior, Comput. Fluids 42 (2011) 37–43, https://doi.org/10.1016/j.compfluid.2010.10.013.
[23] J. Ting, M.W. Peretti, W.B. Eisen, The effect of wake-closure phenomenon on gas atomization performance, Mater. Sci. Eng. A 326 (2002) 110–121, https://doi.org/10.1016/S0921-5093(01)01437-X.
[24] J.S. Thompson, O. Hassan, S.A. Rolland, J. Sienz, LSN Diffusion Ltd, The identification of an accurate simulation approach to predict the effect of operational parameters on the particle size distribution (PSD) of powders produced by an industrial close-coupled gas atomiser, Powder Technol. (2016), https://doi.org/10.1016/j.powtec.2015.12.001.
[25] N. Zeoli, S. Gu, Computational simulation of metal droplet break-up, cooling and solidification during gas atomisation, Comput. Mater. Sci. 43 (2008) 268–278, https://doi.org/10.1016/j.commatsci.2007.10.005.
[26] Y. Shi, W. Lu, W. Sun, S. Zhang, Impact of gas pressure on particle feature in Fe-based amorphous alloy powders via gas atomization: simulation and experiment, J. Mater. Sci. Technol. (2021), https://doi.org/10.1016/j.jmst.2021.06.075.
[27] R. Kaiser, C. Li, S. Yang, D. Lee, A numerical simulation study of the path-resolved breakup behaviors of molten metal in high-pressure gas atomization: with emphasis on the role of shock waves in the gas/molten metal interaction, Adv. Powder Technol. 29 (2018) 623–630, https://doi.org/10.1016/j.apt.2017.12.003.
[28] M. Wei, S. Chen, M. Sun, J. Liang, C. Liu, M. Wang, Atomization simulation and preparation of 24CrNiMoY alloy steel powder using VIGA technology at high gas pressure, Powder Technol. (2020), https://doi.org/10.1016/j.powtec.2020.04.030.
[29] W. Zhao, F. Cao, Z. Ning, G. Zhang, Z. Li, J. Sun, A computational fluid dynamics (CFD) investigation of the flow field and the primary atomization of the close coupled atomizer, Comput. Chem. Eng. 40 (2012) 58–66, https://doi.org/10.1016/j.compchemeng.2012.02.014.
[30] K. Hanthanan Arachchilage, M. Haghshenas, S. Park, L. Zhou, Y. Sohn, B. McWilliams, K. Cho, R. Kumar, Numerical simulation of high-pressure gas atomization of two-phase flow: effect of gas pressure on droplet size distribution, Adv. Powder Technol. 30 (2019) 2726–2732, https://doi.org/10.1016/j.apt.2019.08.019.
[31] Y. Ling, S. Zaleski, R. Scardovelli, Multiscale simulation of atomization with small droplets represented by a Lagrangian point-particle model, Int. J. Multiphase Flow 76 (2015) 122–143, https://doi.org/10.1016/j.ijmultiphaseflow.2015.07.002.
[32] H. Ström, S. Sasic, O. Holm-Christensen, L.J. Shah, Atomizing industrial gas-liquid flows – development of an efficient hybrid VOF-LPT numerical framework, Int. J. Heat Fluid Flow 62 (2016) 104–113, https://doi.org/10.1016/j.ijheatfluidflow.2016.08.007.
[33] D. Zuzio, J.L. Estivalèzes, B. DiPierro, An improved multiscale Eulerian–Lagrangian method for simulation of atomization process, Comput. Fluids 176 (2018) 285–301, https://doi.org/10.1016/j.compfluid.2016.12.018.
[34] S. Luo, H. Wang, Z. Gao, Y. Wu, H. Wang, Interaction between high-velocity gas and liquid in gas atomization revealed by a new coupled simulation model, Mater. Des. 212 (2021), 110264, https://doi.org/10.1016/j.matdes.2021.110264.
[35] J. Anez, A. Ahmed, N. Hecht, B. Duret, J. Reveillon, F.X. Demoulin, Eulerian–Lagrangian spray atomization model coupled with interface capturing method for diesel injectors, Int. J. Multiphase Flow 113 (2019) 325–342, https://doi.org/10.1016/j.ijmultiphaseflow.2018.10.009.
[36] J.M. Desantes, J.M. García-Oliver, J.M. Pastor, I. Olmeda, A. Pandal, B. Naud, LES Eulerian diffuse-interface modeling of fuel dense sprays near- and far-field, Int. J. Multiphase Flow 127 (2020), https://doi.org/10.1016/j.ijmultiphaseflow.2020.103272.
[37] I.E. Anderson, E.M.H. White, R. Dehoff, Feedstock powder processing research needs for additive manufacturing development, Curr. Opin. Solid State Mater. Sci. 22 (2018) 8–15, https://doi.org/10.1016/j.cossms.2018.01.002.
[38] J.P. Choi, G.H. Shin, S. Yang, D.Y. Yang, J.S. Lee, M. Brochu, J.H. Yu, Densification and microstructural investigation of Inconel 718 parts fabricated by selective laser melting, Powder Technol. 310 (2017) 60–66, https://doi.org/10.1016/j.powtec.2017.01.030.
[39] G. Chen, Q. Zhou, S.Y. Zhao, J.O. Yin, P. Tan, Z.F. Li, Y. Ge, J. Wang, H.P. Tang, A pore morphological study of gas-atomized Ti-6Al-4V powders by scanning electron microscopy and synchrotron X-ray computed tomography, Powder Technol. 330 (2018) 425–430, https://doi.org/10.1016/j.powtec.2018.02.053.
[40] L.C. Zhang, W.Y. Xu, Z. Li, L. Zheng, Y.F. Liu, G.Q. Zhang, Characterization of particle shape of nickel-based superalloy powders using image processing techniques, Powder Technol. 395 (2022) 787–801, https://doi.org/10.1016/j.powtec.2021.10.013.
[41] A. Mostafaei, C. Hilla, E.L. Stevens, P. Nandwana, A.M. Elliott, M. Chmielus, Comparison of characterization methods for differently atomized nickel-based alloy 625 powders, Powder Technol. 333 (2018) 180–192, https://doi.org/10.1016/j.powtec.2018.04.014.
[42] Y. Zhao, Y. Cui, Y. Hasebe, H. Bian, K. Yamanaka, K. Aoyagi, T. Hagisawa, A. Chiba, Controlling factors determining flowability of powders for additive

manufacturing: a combined experimental and simulation study, Powder Technol. 393 (2021) 482–493, https://doi.org/10.1016/j.powtec.2021.08.006.
[43] A.K. Pandey, P. Alvaredo, S. Milenkovic, F. Sket, Development of powders of Ti-Fe-Sn ultrafine eutectics for laser additive manufacturing, Powder Technol. 404 (2022), 117416, https://doi.org/10.1016/j.powtec.2022.117416.
[44] E. Urionabarrenetxea, J.M. Martín, A. Avello, Influence of some geometric features of the atomisation chamber on particle agglomeration and aatellite formation during gas atomisation, in: Eur. 2019 Congr. Exhib., European Powder Metallurgy Association (EPMA), Maastricht, Netherlands, 2019.
[45] E. Urionabarrenetxea, J.M. Martín, S. Sainz, A. Avello, Simulation and testing of two different concepts of anti-satellite system for the gas atomisation process, in: Proc. - Euro PM2020 Congr. Exhib., 2020, pp. 1–6.
[46] X.X. Chen, S.J. Tzeng, W.C. Wang, Numerical and experimental observations of the flow field inside a selective laser melting (SLM) chamber through computational fluid dynamics (CFD) and particle image velocimetry (PIV), Powder Technol. 362 (2020) 450–461, https://doi.org/10.1016/j.powtec.2019.11.099.
[47] K. Odum, M. Soshi, K. Yamazaki, Measurement and analysis of impact dynamics suitable for modelling pneumatic transport of metallic powder flow through a directed energy deposition nozzle, Adv. Powder Technol. 33 (2022), 103515, https://doi.org/10.1016/j.apt.2022.103515.
[48] E. Urionabarrenetxea, A. Amatriain, A. Avello, J.M. Martin, Numerical simulation and experimental testing of different close-coupled gas atomiser designs, in: Euro PM 2021 Congr. Exhib., 2021.
[49] E. Urionabarrenetxea, A. Avello, A. Rivas, J.M. Martín, Experimental study of the influence of operational and geometric variables on the powders produced by close-coupled gas atomisation, Mater. Des. 199 (2021), 109441, https://doi.org/10.1016/j.matdes.2020.109441.
[50] TSI Incorporated Press, INSIGHT 3G Data Acquisition, Analysis and Display Sotfware, 2006.
[51] R. Keane, R. Adrian, Optimization of particle image velocimeters. Part I: double pulsed systems, Meas. Sci. Technol. 1 (1990) 1202–1215.
[52] R. Tamura, T. Osada, K. Minagawa, T. Kohata, M. Hirosawa, K. Tsuda, K. Kawagishi, Machine learning-driven optimization in powder manufacturing of Ni co based superalloy, Mater. Des. (2020), 109290, https://doi.org/10.1016/j.matdes.2020.109290.
[53] B. Zheng, E.J. Lavernia, Melt atomization, in: N. Ashgriz (Ed.), Handb. At. Sprays, Springer, 2011, pp. 837–848, https://doi.org/10.1007/978-1-4419-7264-4_36.
[54] R. Ünal, The influence of the pressure formation at the tip of the melt delivery tube on tin powder size and gas/melt ratio in gas atomization method, J. Mater. Process. Technol. 180 (2006) 291–295, https://doi.org/10.1016/j.jmatprotec.2006.06.018.
[55] G. Ni, S. Wang, Q. Li, D. Zhao, C. Song, C. Li, Preparation of Cr17Mn11Mo3N powders by high-pressure gas atomization and the nitrogen increasing mechanism, Powder Technol. 385 (2021) 490–500, https://doi.org/10.1016/j.powtec.2021.03.025.
[56] D.C. Wilcox, Turbulence Modeling for CFD, 2nd ed., DCW Industries, Inc., La Cañada (CA), EEUU, 1998.